

New Strategies for Data Acquisition in Electron Ptychography: Energy Filtering and Reduced Sampling

By MOHAMMAD TAGHI HASHEMI

A Thesis

Submitted to the School of Graduate Studies

in Partial Fulfillment of the Requirements

for the Degree of

Master of Science in

McMaster University

© Copyright by Mohammad Taghi Hashemi, August 2019

Abstract

Electron Ptychography is a technique to retrieve the phase information of the medium through which the electron wave travels in a Transmission Electron Microscope (TEM). Phase calculation is carried out by acquiring an oversampled dataset of diffraction patterns from the sample and execution of a Fourier-based mathematical solution or algorithm using the collected dataset of intensity patterns. The phase of the electron wave contains valuable information about the structure of the material under study. In this contribution, we provide a scientific background necessary for understanding the phase calculation method, examine the capabilities and limitations of the Electron Ptychography in experimental setup and introduce two novel methods to increase the signal to noise ratio by using the same dose budget used in a classic Ptychography experiment.

Acknowledgements

I want to thank Dr. Gianluigi Botton for the trust he had in me as a starting student and for providing me with the opportunity of doing my Master's Degree studies in his group. Indeed, the graduation from Botton's Research Group marks a great achievement in my intellectual life. I also want to thank my group member, Alexandre Pofelski for his generous help, ample inspirations and enormous amount of time he spent with me teaching and discussing a project that was challenging for a new student. I also want to thank both Alexandre Pofelski and Isobel Bicket for helping me learn the intricacies of TEM. I also want to thank the Staff of the Canadian Centre for Electron Microscopy, Andreas Korinek, Carmen Andrei and Andy Duft for their efforts to run this world-class laboratory, especially Andreas for helping me in code optimization. I am thankful of my group members, Hanshuo Liu, Edson Bellido, Sagar Prabhudev, Shayan Mousavi, Viktor Kapetanovic, Reza Safari, Nafiseh Zaker, Eric Daigle and Alfredo Carranco for the great memories they made with me during two year of my studies in Canada.

Table of Contents

Chapter 1: Introduction	1
Chapter 2: A review on how electron microscope functions	5
2.1 Demand for Higher Resolution	6
2.2 Light Microscope and its Limitations	6
2.3 The Advent of Electron Microscope.....	12
2.4 Transmission Electron Microscope and Its Operation Modes.....	14
2.4.1 Parallel Illumination TEM	14
2.4.2 Convergent Beam Scanning TEM	16
2.5 Signals Emanating from Electron-Matter Interactions	19
Chapter 3: Electron Ptychography: Principles and Applications.....	22
3.1 The Phase Problem	23
3.2 Mathematical Treatment of Ptychography	26
3.3 extended Ptychographical Iterative Engine (ePIE) Algorithm.....	35
3.4 Other Phase Retrieval Algorithms.....	39
3.4.1 Wigner Distribution Deconvolution	39
3.4.2 Ptychographical Iterative Engine PIE	42
3.4.3 Super-Resolution extended Ptychographical Iterative Engine SR-ePIE	43
3.5 Pros and Cons of Electron Ptychography.....	47
Chapter 4: Innovative Approaches to Ptychography.....	56
4.1 The concept of Moiré-Ptychography	57
4.2 Energy Filtering of the CBED Patterns.....	65
Chapter 5: Results and Discussion	70
5.1 Experimental Implementation of Energy Filtered CBED Ptychography.....	72
5.2 Resolving Light Atoms.....	77
5.3 The effect of specimen thickness.....	81
5.4 Experimental Implementation of Moiré-Ptychography.....	84
5.5 Ptychographical Reconstruction Troubleshooting.....	85
Chapter 6: Conclusions and Prospects.....	97
Appendix I	101

Appendix II	102
References	104

Chapter 1: Introduction

If we accept the existence of reality outside ourselves, our knowledge of its existence is always second-hand in the sense that the information existing outside needs to be somehow translated and guided through our perception system. If we also accept that whatever we see as an entity in the outside world is just a piece of information, the fact that we feel it with our senses means that the information we received has already been manipulated, since this information has travelled through our nervous system. In fact, this is a huge disconnection between us and the outside world even though we are a part of it. It can hence be argued that if the nervous system does not comprise the entirety of our existence, it stands between us and the pure reality of the world we are living in. In essence, all the means of measurement that we use have a very big limitation; they need to manipulate information in such a way that our nervous system can manipulate it again to understand it. Therefore, although it is absolutely important to always attempt to understand the world better through experience and not solely imagination, it is also critical not to forget that our knowledge gained through characterization would never be synonymous with the reality.

All the attempts made in the history of the field of microscopy were only intended to gain the information that we cannot access directly by our senses. The instruments used for probing the information we need always lose and alter information as they are measuring, just as our bodily senses do. In the context of Electron Microscopy, which is essentially probing matter with electron waves, a greatly valuable piece of information is lost through the acquisition process: the phase of the wave. In other words, we are

currently capable of measuring only the intensity (amplitude squared) of the waves scattered from the process of probing matter inside an electron microscope. The phase cannot be measured directly; this concept is called the phase problem and will be discussed in more detail in the rest of this thesis. In a nutshell, Electron Ptychography is an attempt to retrieve the lost phase of the electron wave by making use of multiple intensity measurements.

Retrieving the phase of the wave by using multiple intensity pattern measurements is only possible if the phase of the wave is encoded in the intensity. The way this encoding is done is by using the *Interference* phenomenon. When interference of two waves happens, the phase information of rays determines the amplitude of the resultant wave. Encoding the phase information is thus rendered possible by recording the intensity of the interference pattern (or the amplitude square). For a meaningful and interpretable interference, the waves interfering should be *Coherent*. Coherence in this context means that the phases of the waves interfering are correlated. *Coherent Diffraction Imaging* is based on the concept of retrieving the phase information by interference happening in the diffraction pattern. Ptychography is a sub-category of CDI and Electron Ptychography is using the Ptychography principles of phase calculation in the context of Electron Microscopy.

Calculation of the phase information in Electron Ptychography used in the results of this thesis begins with recording 2D diffractions patterns from a 2D set of scanning points

from a sample under a convergent beam of probing electrons which makes up a 4D (2Dx2D) dataset of diffraction patterns. Afterwards, a specific function shape is assigned to the probing electrons (probe) and the sample (object) and the diffraction pattern created by the interaction of these initial estimated functions is mathematically modeled. At each step of the phase calculation, the diffraction pattern calculated is refined by altering the probe and object functions such that the diffraction pattern calculated in the next step is more similar to the diffraction pattern recorded from the sample. The convergence of the phase retrieval algorithm is confirmed when the diffraction pattern calculated from the object and the probe functions calculated is almost identical to the diffraction pattern physically recorded.

The outline for this thesis will be the following. The chapter 2 attempts to explain the basics and operation principles of Electron Microscope to the extent that is needed for further discussions. A brief history of microscopy, the concept of resolution, barriers of achieving higher resolution and the interaction of probing electrons with matter are discussed. In chapter 3, phase problems and different approaches to solving it are discussed. Chapter 4 is introducing two novel approaches to electron Ptychography; one concerning extending the application of Ptychography to thicker samples and the other increasing the dose efficiency of Ptychography. In chapter 5, implementations of electron Ptychography are examined and the sensitivity of the technique to different experiment and phase reconstruction parameters are deliberated.

Chapter 2: A review on how electron microscope functions

2.1 Demand for Higher Resolution

Material properties are linked to their structure. It's ultimately the geometrical arrangement of around 100 elements of the periodic table that make up all the materials and their behavior. The logic follows that if we as human beings want to use or alter materials to our benefit, we need to study the building blocks of matter in order to fully grasp the essence of the properties. The building blocks of matter, whether atoms or the microstructures they create, are smaller than what a human eye can see. The average minimum distance a human eye can resolve is 0.1 mm [1]. This is orders of magnitude more than, say, the size of the atom ($\sim 1\text{\AA}$) or the grains in a metallic structure (μm). Therefore, the need for a microscope to assist visualizing these structures is inevitable.

2.2 Light Microscope and its Limitations

The oldest lens discovered, dates back to 721-705 B.C. [1]. It has been found in the palace of Assyrian emperor Nimrud. The so called "Nimrud Lens" was ground and polished from a transparent rock crystal. It is not until the first century A.D. that Seneca introduces the concept of magnification by a water filled globe. Around one thousand years later, Ibn al-Haytham studied the structure of the eye and how the lenses in the human eye focus the light on the retina. The first widespread application of lenses was reported to happen in 1280 A.D in Florence with the invent of eyeglasses [1].

The invention of the first microscope having more than one lens is accredited to Hans Jansen around 1595 A.D. The maximum magnification achieved by this microscope is reported to be 9X when fully extended (18 inches). Although mechanical improvements in 18th century led to a resolution of 5 μ m, the images were distorted in many ways. Colour haloes and blur were making the fine features of the image indistinguishable. The problem of lens distortions was alleviated by a method proposed by Lister in 1830, 235 years after the advent of the first microscope [1]. This implies that it took around two centuries for the early scientists and microscopists to understand the complex nature of lens induced image distortions.

These distortions directly stem from the geometry and imperfections of a round lens, which cause the rays coming from a point in the object to not be focused to a point in the image plane. In principle, the rays emanating from a point in the object, regardless of their colour, angle or distance from optic axis, should be focused to a point in the image plane by a perfect lens. In reality though, a round lens is unable to focus the parallel rays to exactly a single point to do so due to its inherent geometry and imperfections. The situation is exacerbated in a microscope since more lenses are involved in order to have a high enough magnification and hence, these lens' errors compile. In a nutshell, parallel rays arriving at a lens, regardless of their colour, incident angle or distance from optics should be focused to a point in the focal plane. The inability of a lens for correctly doing so is attributed to lens errors that are called *aberrations* of the lens.

Among several types of lens aberrations, the most impactful ones are *Chromatic* and *Spherical* aberrations. Chromatic aberration is the inability of a lens to focus a multi-coloured point source into a point in the image plane. Due to the lens' varying refractive index for different wavelengths of light, the angle with which rays exit the lens will not be identical. In other words, light rays with higher wavelength focus earlier (or closer to lens) compared to lights with lower wavelength as depicted in Figure 2.1.A adapted from [2]. At the image plane, this effect is seen as one colour being focused to a point and the other forming a halo. The spherical aberration is similar to chromatic aberration in the final effect, but it affects the rays travelling farther from the optic axis as shown in Figure 2.1.B adapted from [3]. The farther the beams are located from the optic axis, the closer to lens they are focused by the convex lens because of the higher radius of the curvature at marginal areas.

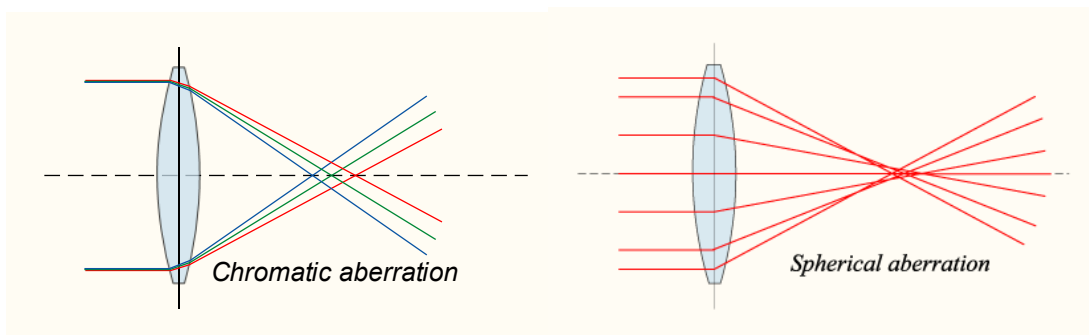


Figure 2.1. A) Chromatic (adapted from [2]) and B) Spherical (adapted from [3]) Aberrations

The criterion mentioned earlier about the ability of a lens to focus a point to another point (and not a circle) holds true only if the wave nature of the light is neglected. If light is of totally corpuscular (or particle) nature, the quality of the final image created

by a lens should only be dependent on the precision of optical system manufacturing; a belief held by scientist until mid-19th century. Although the geometry of ray pathways in this criterion guarantees that a point is focused into another point, taking the wave interference into account, it doesn't guarantee that the interference would be constructive at that point. In fact, Abbe showed in 1873 that even in an aberration free lens system, it is impossible to completely focus rays of light to a point due to the existence of the diffraction phenomenon [4].

Historically, it is the observation of diffraction that undermines the Newton's well established corpuscular light theory that was based on his laws of motion. Observations of Girmaldi (1813-63), Hooke (1635-1703) and ultimately, the irrefutable experiments of Young in 1801 [4], could not be explained by assuming a particle nature for light.

The diffraction phenomenon happens when the pathway of light is confined by or passes from the vicinity of an obstacle of any sort. Interaction of the light wave with the edge of the obstacle induces a phase change in rays passing nearby the edges. Travelling rays interfere with one another and if a camera is placed in the pathway, an interference pattern is observed at any given distance from the obstacle. Similar to Young's double slit experiment, if an obstacle with a circular hole of diameter D (an *aperture*) is placed in front of a coherent (wavelength invariant) parallel beam of light, interference in a plane far away from the aperture (or at the focal plane of the lens) will resemble a set of concentric circles, as shown in Figure 2.2.

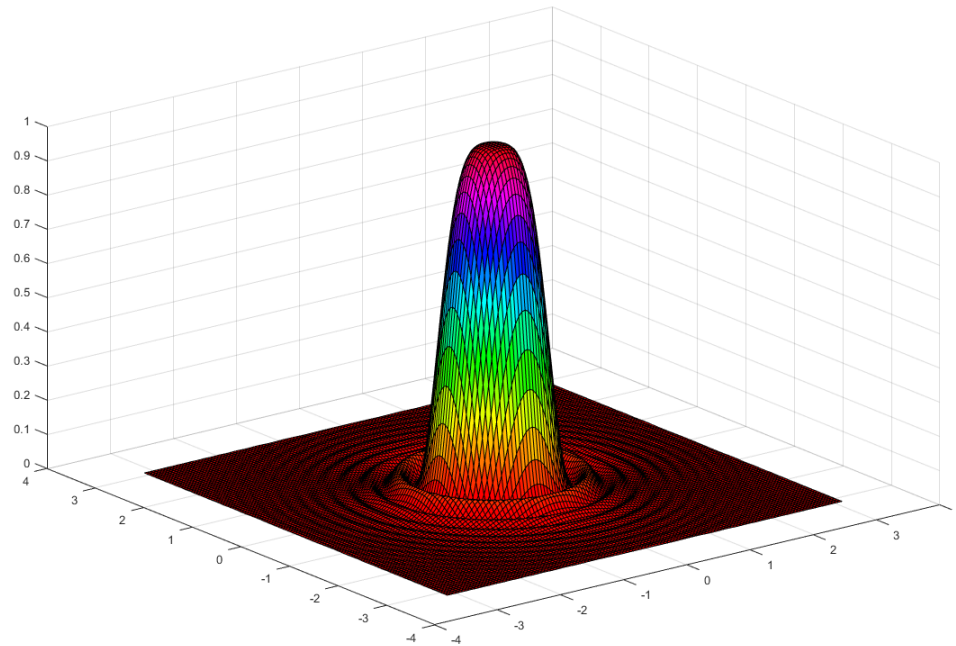


Figure 2.2. Intensity of the wave diffracted from a circular aperture (X & Y: Space coordinates and Z: Intensity of light)

The 3D representation of the interference pattern shown in Figure 2.2 is called an Airy pattern (or Airy disks). The diameter of the central disk would be $1.22\lambda/D$ with λ being wavelength of the illumination. In a case of two apertures with a varying distance δ between centers, there is a minimum distance below which it is impossible to regard them as two disks in the image due to the interference pattern formed. This minimum distance is chosen to be $0.61 \lambda/D$, which is the radius of the disk, by Rayleigh criterion as shown in Figure 2.3 [5]. The implication is that, because of diffraction, rays emitted from a tiny aperture (a point source) are focused into Airy disks (not another point!). This entails that diffraction poses a physical limit on image formation even in absence of any lens

aberrations or in a lens-less configuration. For visible light, the physical limit of resolution due to presence of Airy disks would be around 200 nm. One could argue that without an aperture in an optical system, focusing confusion arising from diffraction could be eliminated but indeed, the use of an aperture is inevitable in presence of aberrations. A more quantitative explanation of diffraction from matter will be presented in Chapter 3.

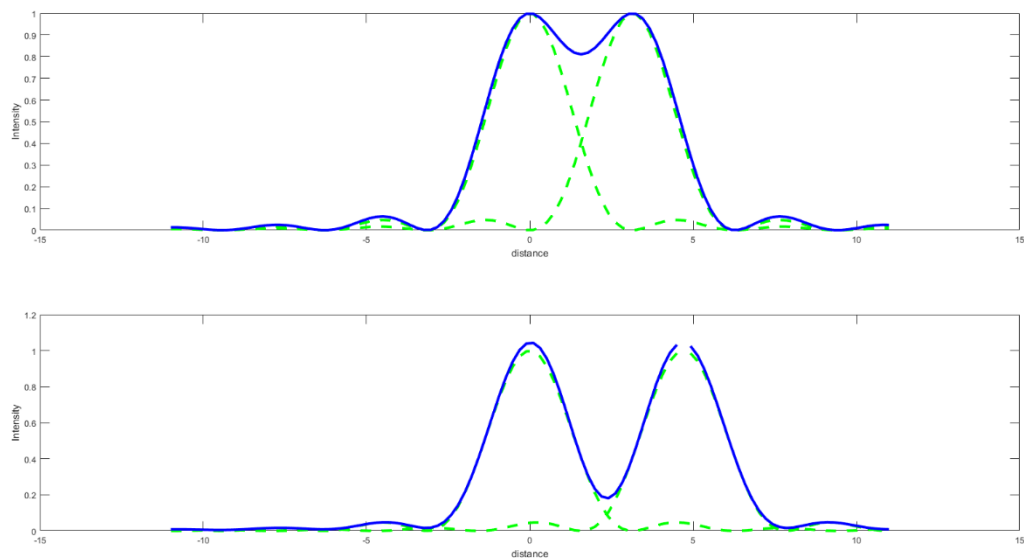


Figure 2.3. Each green dotted line represents a point source and the solid blue line represents the addition of the two intensities. When closer than $D/2$, distinction between them would be hard.

By definition, *resolution* is the distance between two points in an image below which it is impossible to recognize them as two separate items [5]. In other words, resolution is the measure of how fine the details are in an image. In the absence of lens aberrations, resolution is dependent on the diffraction limit which is proportional to the wavelength of the probing wave. Therefore, the lower the wavelength, the lower (and better) the resolution would be. It is also inversely proportional to the diameter of the

(numerical) aperture. It is beneficial for the resolution to increase the range of angles the optical system accepts by increasing aperture diameter, but by doing so, *temporal* and *spatial coherence* of the beam are lost (chromatic, spherical and other types of aberrations are introduced).

2.3 The Advent of Electron Microscope

As mentioned earlier in the very brief history of light microscopy, magnifying lenses were invented way before there were any scientific explanation of how they work. For the case of electron microscope, it was the opposite. Historically, the idea of using electrons as a probing wave for studying materials was derived from Louis De Broglie's theorem of matter waves [6]. In 1932, he proposed that for a particle with momentum p , the wavelength associated with it would be

$$\lambda = \frac{h}{p} \quad \text{Eq. (2.1)}$$

Where h is the Planck's constant. Therefore, the immediate result of this would be for an electron having a measurable mass and high speed, the wavelength would be very small compared to light (400-700 nm). For a beam of electrons travelling with 300 KeV of energy (conventionally used in current transmission electron microscopes), the de Broglie's wavelength would be 1.9 picometers, around one hundred thousand times smaller than the wavelength of visible light. This is physically a promising wavelength to study the materials well below nanometer region.

This triggered a set of theoretical and experimental efforts in the history of the electron microscopy. The idea was to use an electron emitting sources instead of electromagnetic wave emitters, which had been formerly examined by J.J. Thomson. The development of electron lenses (which are essentially magnetic or electrostatic coils) and theoretical electron optics throughout the 1920s led to construction of the first Transmission Electron Microscope (TEM) by Ernst Ruska in 1933. This microscope demonstrated a 12,000X magnification with a better resolution than a light microscope [6].

Since then, there have been many advancements in the field of electron microscopy to get the achievable resolution closer to the physical limit. Addressing electromagnetic lens aberrations, development of means of thin sample preparation (Ultramicrotome), development of brighter electron sources, commercializing the TEM and construction of the first SEM are some of developments occurred prior to year 1970 [6].

After 1970, the development of aberration corrector optics and lenses, *Electron Energy Loss Spectroscopy (EELS)*, theory and application of *Scanning Transmission Electron Microscopy* are some of the most highlighted events in the following years [6].

2.4 Transmission Electron Microscope and Its Operation Modes

The TEM is currently one of most intensively used characterization machines in Materials Science and related fields. Due to its high resolution and the great wealth of chemical and crystallographic information it can provide, it has been an indispensable equipment for materials characterization. There are two most commonly used modes of operation for this device; namely TEM (or parallel illumination) and STEM (or Scanning mode). A summary of operation mechanisms for these modes is provided in the following text.

2.4.1 Parallel Illumination TEM

In the TEM mode, a thin sample (below 100 nm) is shined upon by a stream of accelerated, high energy (>60 KeV) electrons that have been emitted by an electron source (*Electron Gun*). A set of magnetic lenses and electron beam (*e-beam*) deflectors (called the *Condenser System*) are responsible to deliver a demagnified image of the electron source to the *Objective Lens*. The objective lens is to fashion the electron beam into a desired shape and deliver it to the sample which, in the case of TEM, would be a broad and ideally parallel illumination. After the e-beam passes through the sample, the electrons are projected to a detector plane by the *Projector System (or Imaging Lenses)*. A portion of the electrons which may or may not have interacted with the sample is then collected by an *Electron Detector* as a signal. This signal carries chemical and structural

information about the material under study. At the end of the *Electron Column*, electrons may end up on the surface of a Charge-Coupled Device (CCD) or can enter the EELS Spectrometer for chemical analysis. Two parallel illumination TEM modes and a schematic diagram of how the imaging lenses lead the beam is represented in Figure 2.4. adapted from [7].

As Figure 2.4.A shows, the parallel diffracted rays from a sample are focused into one point (a small disk!) in the Back Focal Plane (BFP) of the objective lens. The pattern created by these dots is called diffraction pattern. The diffraction pattern is located at the object plane of the imaging lenses in this mode. Therefore, a magnified image of it is projected on the Viewing Screen (Phosphorous Screen) or Camera.

In the mode shown by Figure 2.4.B, the rays which met at the diffraction spots continue their way to meet and interfere once again in the image plane of the objective lens. Thus, an image of the object is in this plane. This could also be seen by following back the rays coming from the same point in the sample. Now the image plane of the objective lens serves as the object plane for the rest of the imaging system. Finally, an interference pattern (image of the sample) is formed on the screen. This extra interference step is an important concept which will be addressed once again in chapter 3.

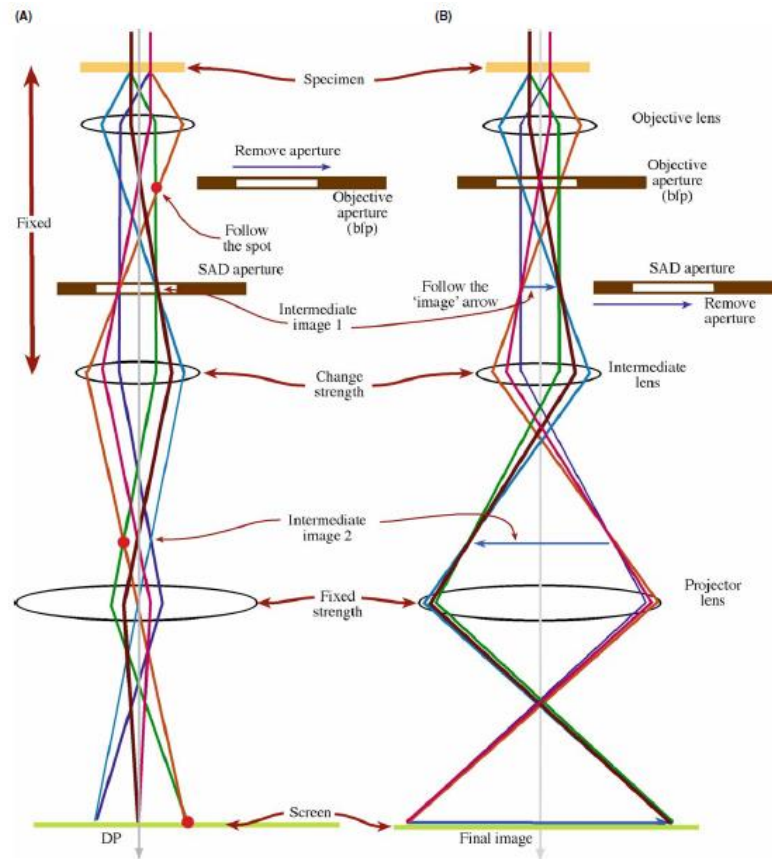


Figure 2.4. parallel illumination modes of TEM A) Diffraction and B) Imaging [7]

Along the way, there are apertures to limit the range of angles within which the rays are accepted. The *Objective* and *Selected Area Apertures* are located in the BFP and Image plane of the objective lens respectively.

2.4.2 Convergent Beam Scanning TEM

As the name implies, the illumination and signal acquisition methods are different in this mode of operation. In a nutshell, this mode is based on scanning a small convergent (as opposed to parallel) beam of electrons on the sample and collecting a signal point-by-

point and reconstructing the image of the area scanned from the signal collected. The necessity of using a convergent beam is that strong lenses are needed to focus electrons on a sample. The stronger the electromagnetic field of lens, the closer the focal point would be to the lens and thus, the higher the convergence angle. The aftermath of having a convergent beam illumination would be that the diffracted beams, especially from a crystal, would have the same range of angles as the beam. In other words, diffraction spots turn into disks (diffraction disks get bigger to be precise!). A schematic diagram is shown in Figure 2.5 adapted from [7].

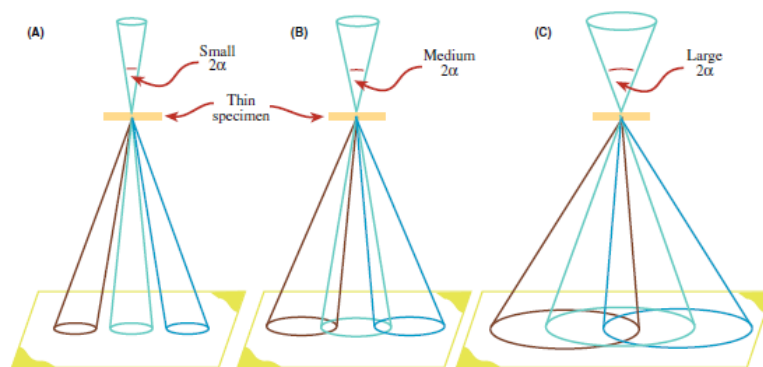


Figure 2.5. Increase of diffraction disks' diameters due to increase in convergence angle of the beam (α) [7]

For having atomic resolution in STEM, it is mathematically proven that the convergence angle must have such a condition that the diffracted beams overlap [8]. For certain, this is a necessary and not a sufficient condition. The diffracted beams may be collected in whole or in part by a CCD camera or an annular detector. An annular detector is an electron sensor which has a hole of certain diameter in the center. This allows the

non- or slightly- diffracted electrons to pass for further analysis (e.g. EELS) and records the current of electrons in a range of angles usually measured in milliradians (mrad).

There are several advantages of STEM over TEM mode. Site specificity of the signal, exclusion of imaging lens system and removing its accompanying aberrations and availability of signal in high scattering angles are to name but a few. Since the CBED is formed after the sample, the user of the microscope is free to choose which portion of the signal they are willing to use. If a contrast arising from the atomic number in the specimen is desired, the *High Angle Annular Dark Field* detector could be used. This detector permits a certain range of angles in the signal to transfer and collects the higher-angle scattered electrons. By integrating the collected electrons for each scanned pixel, an HAADF image is formed. The usual range of angles for this detector is >50 mrad [7]. In case visualization of lighter atomic columns is intended, a range of angles (11 to 22 mrad) [9] in the CBED could be used. By integration of signal in this angle range, an image is formed where the contrast is more sensitive to light atomic columns since the lighter atoms are weaker electron scatterers than heavy atoms and the information is expected to be found in lower scattering angle ranges. This technique, as would be referred to in chapter 3, is defocus and thickness dependent to a high degree. This means optimal experimental conditions are needed to have an interpretable contrast in the image which may not be feasible with regards to time and sample. A schematic illustration of the electron signal collection angles is represented in Figure 2.6 adapted from [9]. The range of angles determines the contrast mechanism. For 0 to 11 mrad integration angle, the

imaging contrast is called Bright Field, for 11 to 22 mrad we have the Annular Bright Field region, while the 22 to 50 mrad range is considered Annular Dark Field region and more than 50 mrad, we have the HAADF signal.

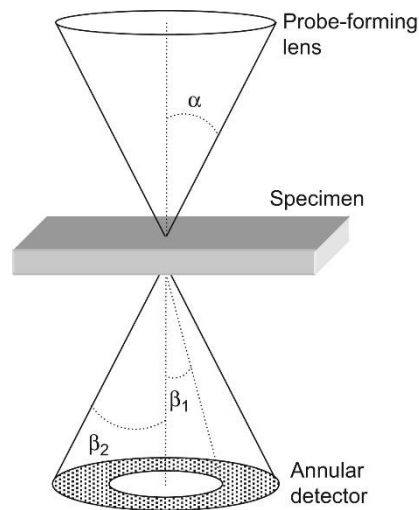


Figure 2.6. Annular detector setting [9]

2.5 Signals Emanating from Electron-Matter Interactions

When the e-beam is directed to the sample, the electrons are interacting with the potential of the sample and experience different interactions throughout their passage. As a result of these interactions, the energy and/or momentum vector of the electrons may be altered. Interactions of incident electrons and the atoms of the sample can be categorized into different groups as presented in Table 2.1.

Among all the information signals, we are interested in the first four in table 2.1 for later discussions. The *Direct beam* is referred to the primary e-beam electrons which had minimum interaction with the sample. These electrons will not deviate from their initial pathway and exit the sample with the same trajectory. *Elastically scattered electrons* experience a momentum vector alteration by the atomic potential, but do not lose a considerable amount of their energy. If the momentum transfer vector is of small magnitude, the phase relation between the scattered electrons remains correlated (assuming they are emitted coherently from a source). The term *Coherent Elastic*, therefore, stems from conservation of phase relation. On the other hand, if the momentum transfer vector's magnitude is substantial, the phase relation between these electrons is lost. Therefore, *Incoherent Elastic* term is assigned to these types of interactions.

The last types of interactions falling into the scope of this writing are *Incoherent Inelastic* events. These electrons collide with the atomic inner shell electrons and cause the tightly bound electrons of the atom to go to higher energy states. Hence, electrons lose a portion of their initial energy. Having experienced both energy and momentum change, the phase relation between them is disassembled. Therefore, these interactions are called *Incoherent Inelastic* collisions.

Table 2.1. Signals coming out of electron-matter interaction sites

#	Name	Description	Contained Information	Primary/Secondary	Range of Angles
1	Direct Beam	Electrons that had minimum or no interaction with the sample	Energy spread of the beam	Primary	$<1^\circ$
2	Coherent Elastic	Electrons experiencing almost no energy transfer and small momentum transfer	Diffraction	Primary	$1^\circ \ll 10^\circ$
3	Incoherent Elastic	Electrons experiencing almost no energy transfer and big momentum transfer	High angle Z-contrast information	Primary	$10^\circ <$
4	Incoherent Inelastic	Electrons experiencing both energy and momentum transfer	Chemical and band structure	Primary	$<1^\circ$
5	Secondary e^- (SE)	Electrons ejected from atoms as a result high energy beam electron impact	Surface topology	Secondary	360°
6	Back Scattered e^- (BSE)	Electrons of the primary beam experiencing a scattering event having angles more than 90° coming out of the sample	Chemical and Surface Topology Information	Primary	$90^\circ \ll 270^\circ$
7	Auger Electrons	X-Ray photo-electrons ejected by the collision of X-Ray photons	Chemical	Secondary	360°
8	X-Rays	X-Rays emitted as a result of inner-shell ionization of atoms by incoming electrons	Chemical	Secondary	360°

Here, the idea of electron wave's phase and phase relation was mentioned. It is important to define these terms and determine how the phase could be beneficial for having a better resolution. Chapter 3 is an attempt to look into the concept of phase and inspect the advantages of knowing it.

Chapter 3: Electron Ptychography: Principles and Applications

3.1 The Phase Problem

Matter is composed of atoms; which essentially is a package of electrically charged particles. The positioning of these charged particles in the vicinity of each other creates a potential field in the space. When the atoms bond to make solid matter, the relative distance of the atom cores and the charge distribution in the space occupied by the matter, determine the atomic potential field of the matter. Therefore, the matter can be viewed as a potential distribution in 3D space which is described by a function $V(x, y, z)$. This function encompasses all the necessary information about the structure and chemistry of the matter. Therefore, the ultimate goal of microscopy is to recover (or reconstruct) this function with desired resolution by probing it by a certain means. This probing could only happen with an article that is meaningfully interacting with this electric potential; else, it would not be affected and the final signal will always be the same regardless of the sample. That is why electromagnetic waves and electrons are good candidates to be used in microscopes. After the interaction has happened, a model is needed to relate the result of the experiment (or the collected signal) to the atomic potential. In this sense, the problem is an Inverse Problem [10].

As mentioned in the previous chapter, the electron beam propagating through the microscope is of a wave nature. As this wave propagates through matter (i.e. the specimen), it experiences an Amplitude and Phase change. This change stems from the interaction of probing electrons with $V(x, y, z)$. Assuming the initial beam of electrons is

fully coherent and monochromatic, by measuring the relative phase and amplitude change after the interaction, the atomic potential function can be calculated or reconstructed without any ambiguity. Unfortunately, this is not currently possible since the electron (and light) detectors are only capable of measuring the Intensity of the wave, which is the wave's amplitude squared. In other terms, the phase information is conserved throughout the whole processes happening in the (ideal) microscope, except the last moment when the final measurement is performed by the detector. After the measurement, a complex valued wave function transforms into a fully real function (a 2D image). If solving for the phase is now what is intended, an infinite number of complex valued functions exist to correspond to the same amplitude distribution. Thus, a unique solution for the phase does not exist due to phase information loss on the detector. This is regarded as the Phase Problem and attempts to solve for this phase ambiguity problem are termed Phase Retrieval methods [11].

Since only the amplitude squared of the electron wave can be recorded experimentally, a solution shall be found for calculating the phase of the wave having only the intensity patterns. One approach is to design an experiment such that the phase is calculated by measuring a set of intensity patterns. *Coherent Diffraction Imaging (CDI)* is a technique adopting this approach. CDI is based upon collecting an *oversampled* or *redundant* set of Far-Field diffraction patterns from an object and reconstruction of the phase using Fourier based algorithms. There exist four categories of CDI: Plane-Wave CDI, Ptychographic CDI, Bragg CDI and Fresnel CDI [12]. Having the same principle and

reconstruction algorithms, these techniques differ in the way of data collection (scanning vs. sample tilting) or their scope (nanocrystals vs. extended object). The great advantage of CDI is that it does not require any lenses to create the diffraction spots to interfere to create an image and it is called a lens-less technique in this sense. That is best seen when a Fourier transform of a high resolution TEM image is made. In the original diffraction pattern, the number of spots or the range of angles (frequencies) present is much larger compared to the Fourier transform of the image; signifying that high frequency information is lost in the process of recombining diffracted waves in the real space by imaging lenses. This makes CDI a powerful technique since it requires no imaging lenses in principle. However, the main limitation would be the detector recording the diffraction patterns.

Alongside the coherence of the probing beam being required, the detector must have certain characteristics for a valid data acquisition. Firstly, it should possess a high *dynamic range* since the center beam is several orders of magnitude brighter than the diffracted beams, even for crystalline samples (i.e. the detector should be capable of recording both low and high frequency information at the same time). Secondly, a high *quantum efficiency* is required since the diffracted beams, specially the higher order ones, are of very low intensity. Thirdly, the *noise* level (dark, thermal, etc.) should be kept low to the best possible extent. Otherwise, the high frequency information that is vital for a high resolution, are lost in the noise due to their low intensity. Finally, the acquisition time or *frame rate* should be fast enough to prevent beam damage to the sample. This is crucial

in a Ptychography experiment (explained further below) since the electron beam damage is exacerbated due to the redundancy of data collection. All these criteria underline the key importance of the detector for acquiring a good dataset for CDI.

The focus of this chapter is *Electron Ptychography* which is fundamentally a CDI technique particularly adapted to the electron microscope. This technique is based on collection of 2D diffraction patterns from a 2D scanning grid, making up a *4D dataset*. Subsequently, this dataset is fed into a phase retrieval algorithm to reconstruct the complex valued function of the object under examination. The following section seeks to explain how the phase reconstruction of the object is constituted mathematically.

3.2 Mathematical Treatment of Ptychography

As mentioned earlier, the electron beam used in a TEM can be considered a wave. A mathematical expression could be proposed to define the amplitude and phase of this wave entirely throughout the space and time domains. Since we assume that the electron signal collected is invariant with time, we are only interested in the time-independent waveform. We will follow hereafter the derivation of Ptychographical phase reconstruction theory as presented in reference [13]. As the general form of a wave vector we have [13]:

$$\psi(x, y) = a(x, y)e^{-i\varphi(x, y)} \quad \text{Eq. (3.1)}$$

The 2D wave $\psi(x, y)$ has an amplitude $a(x, y)$ and a phase $\varphi(x, y)$ at every point (x, y) in space. This wave is diffracted by a crystal (a crystalline sample is assumed for

simplicity of expression). The diffraction pattern is consisting of a non-diffracted or direct beam called " O " and a set of diffracted beams called " $V_{n,m}$ " which " n " and " m " are integers indexing the location of the diffracted beam. O and $V_{n,m}$ have an amplitude and a phase component assigned to them. Thus, if N diffraction spots exist in the diffraction pattern, $2N$ parameters should be calculated to reach a complex valued solution. Although knowing the absolute phase may be interesting from a physicist's point of view, it may not be as important for a microscopists. Microscopy is interested in the structure, which is information regarding relative positions of atoms. It is not necessary for studying the structure of the material to exactly know how much a certain atomic column has changed the phase of the probing wave. However, it is important to know how much each atomic column has change the phase compared to other atomic columns. Consequently, it is assumed that the central beam has a zero phase component and the phase of other diffracted beams are measured relative to this non-diffracted beam.

This individually does not solve the problem since we have N measurement of the amplitude squared, but $2N - 1$ variables to solve for the whole diffraction pattern. The key to the solution is to increase the ratio of measured (intensities) to unknown variables. For the simple case of two beams, making two beams interfere provides an additional information as shown in Figure 3.1.A inspired from [13]. In the simple two beam case demonstrated, the unknown variables would be the phase and amplitude of O and V . By assuming the phase of O is zero, we have three variables to solve for. If the two beams are not interfering, we would have two intensity measurements and three variables which

will not provide a unique solution for the phase problem. By letting them interfere, measurement of three intensities is done which leads closer to a unique solution. As seen in Figure 3.1.A, two intensities of individual beams and one *double overlap* region can be measured. For the case in which three beams are involved, at least five intensity measurements are needed which will be provided with the experimental setting shown in Figure 3.1.B inspired from [13]. Three individual, three double overlap and one triple overlap regions can be measured.

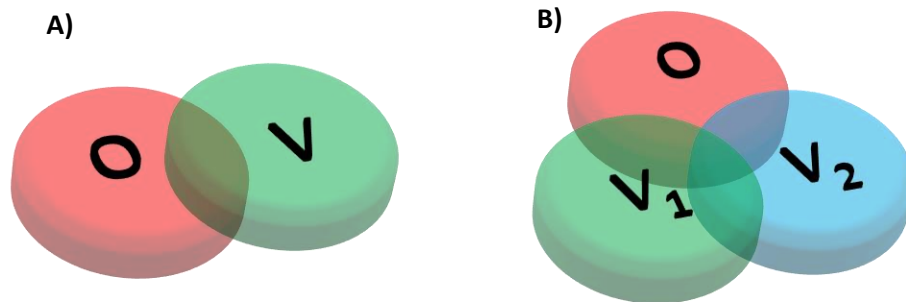


Figure 3.1 Overlap of A) two and B) three diffracted beams, increasing ratio of number measurements to unknown variables

This discussion illustrates why beam overlap is needed for Ptychographical reconstruction. In fact, by choosing a proper convergence angle in CBED acquisition, the desired overlap would be achieved as described in section 2.4.2 inspired from [13]. Although the ratio of measurements to variables is increased, the solution would have another uncertainty which is the sign of the phase (as exhibited in Figure 3.2.A).

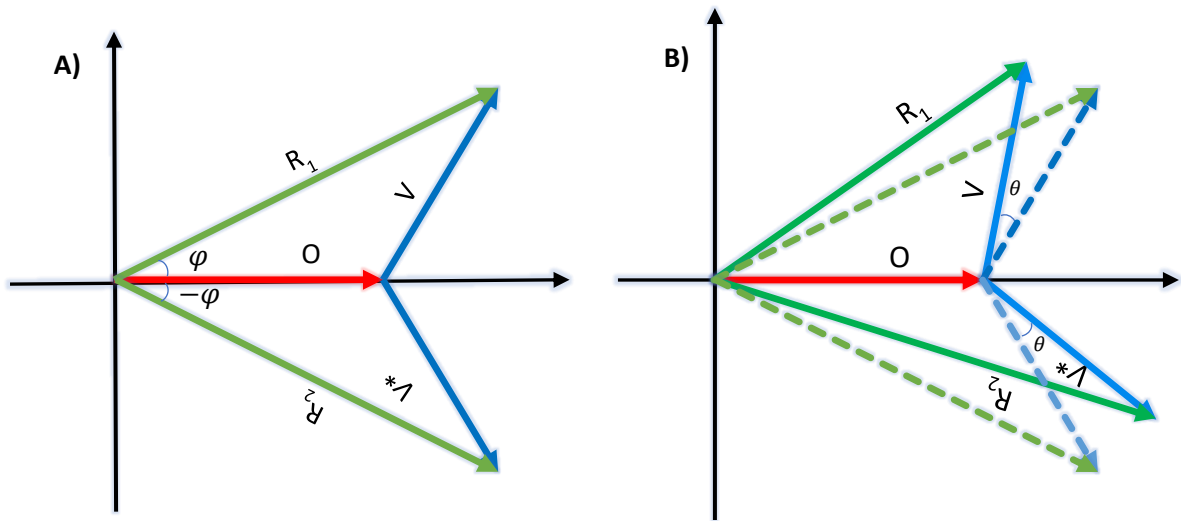


Figure 3.2 A) Uncertainty in phase of V B) Another measurement with beam tilt to remove the phase uncertainty

By measuring the intensity of O and V and their overlap region R , there would be two possible R_1 and R_2 vectors that are equal in amplitude, but opposite in phase. In other words, R_1 would be $O+V$ and R_2 would be $O+V^*$ (V^* is the complex conjugate of V). With this measurement, therefore, the total uncertainty in phase of the vector V comes down to two values φ and $-\varphi$.

A way to remove this last uncertainty is to tilt O and V vectors by an equal angle θ . By doing so, R_1 and R_2 which previously had identical magnitudes, will differ in magnitude. By measuring the intensity of the overlap in this setting, the uncertainty of the phase is totally resolved. It is worthy of note that the coordinate reference is also tilted by θ in Figure 3.2.B. How this solution could be achieved in the experimental conditions is an important matter. The experimental implementation is enacted by introducing a beam tilt relative to the optic axis of the microscope. A shift of the

illumination in real space caused by beam tilt would introduce a *Linear Phase Ramp* on the central and diffracted beams in the diffraction space. A linear phase ramp will break the symmetry in the two halves of the beams. One side of the beam will advance in phase and the other will recede. This can be described by multiplication of $e^{i\theta}$ to the reciprocal space function. Therefore, the intensity of the overlap section measured would be the amplitude squared of the vector $Oe^{-i\theta} + Ve^{i\theta}$ as shown in Figure 3.3 inspired from [13].

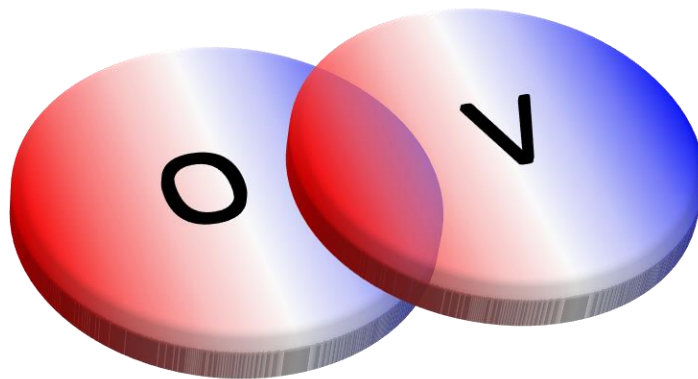


Figure 3.3. Overlap of the central and diffracted beams in the presence of beam tilt.

In STEM configuration, this beam tilt is carried out by STEM scanning coils. In fact, for rastering the beam on the sample, scanning coils tilt the beam in increments to generate the beam shift. This experimental set-up would create conditions similar to those explained in Figure 3.2.B. With another measurement added, solving for the phase of the diffracted beams is possible. Here, we underlined the necessity of multiple measurements and convergence of the incident beam in Ptychography. In order to provide a connection between these intensity measurements and the structure of the material, the mathematical model used by Ptychography literature is explained below.

As expressed earlier, the incoming wave of electrons is modified by the atomic potential of the matter. After this modification, an *Exit-Wave* is formed which then progresses down the TEM column. The interaction of the beam and specimen is modeled by Eq. 3.2 [13] [14].

$$\psi_e(x, y) = a(x, y) \cdot o(x, y) \quad \text{Eq. (3.2)}$$

The expression of the exit-wave $\psi_e(x, y)$, is the multiplication of $a(x, y)$ which is the illumination wave in real space (or the *Probe Function*) and $o(x, y)$ which is the *Object Transmission Function*. Both functions are complex valued and are of the waveform described by Eq. 3.1. The important note about $o(x, y)$ is that it is not the atomic potential function, but it is only a function to describe how the substance is changing the amplitude and phase of the electron wave. Hereby, a multiplicative behavior of the object function is assumed. This implies that the object is thin enough that the diffuse scattering and dynamical diffraction phenomena are negligible. Otherwise, this equation must be augmented by other terms and functions to account for these phenomena.

The exit-wave is refocused by a set of lenses (imaging lenses) to form the diffraction pattern. According to Fraunhofer theory of diffraction, this diffraction pattern created by lenses is equivalent to the diffraction pattern in the far field (a plane located at infinity) without lenses. The amplitude of the wave at infinity (or *Far-Field*) can be modeled by a 2D (*Forward*) *Fourier Transform* [15]. According to *Fourier Inversion Theorem*, for estimating the amplitude and phase of the source wave from the complex

valued wave function in far-field, a *Backward Fourier Transform* is performed. The formulae of both these integral transforms are included in Appendix I.

The e-beam in STEM is positioned in real space and since it is formed by a lens, its origin should be lying in the reciprocal space by reciprocity principle. This origin is the numerical or physical aperture of the probe forming lenses. It is beneficial to describe the aperture function as $A(u, v)$ where (u, v) are the indices of the reciprocal space. The diffraction lenses project a far-field pattern on the detector and, mathematically, this behavior can be described by a forward Fourier transform. Given that the exit-wave is the result of multiplication between probe and object function in real space, according to the *Convolution Theorem*, the Fourier transform of it would be the convolution of Fourier transforms of each function in reciprocal space (see Appendix I) [13]. Therefore, the intensity of the diffraction pattern would be the amplitude squared of the convolution of the aperture function and the *reciprocal lattice transmission function* [13]:

$$I(u, v) = |A(u, v) * O(u, v)|^2 \quad \text{Eq. (3.3)}$$

The reciprocal lattice Transmission Function can be modeled as [13]:

$$O(u, v) = \sum_{n,m} O_{n,m} \delta(u - nu_0, v - mv_0) \quad \text{Eq. (3.4)}$$

u_0 and v_0 being unit reciprocal lattice vectors. The implication is that the whole reciprocal lattice can be formed by a linear combination of these unit vectors. $O_{n,m}$ is the complex amplitude of the reciprocal lattice transmission function. The use of *Dirac Delta*

Function (see Appendix I) has some interesting properties which later helps the solution of the phase equations. The delta function pegs $O_{n,m}$ the location of the reciprocal lattice.

Having $O(u, v)$ defined by Eq.3.4, Eq.3.3 can be redrafted as Eq.3.5 due to *Sifting Property* (Appendix I) [13]:

$$I(u, v) = \left| \sum_{n,m} O_{n,m} A(u - nu_0, v - mv_0) \right|^2 \quad \text{Eq. (3.5)}$$

Referring to the problem discussed earlier in this chapter, regarding only two beams located on x-axis, the two intensity measurements would be mathematically expressed as [13]:

$$I_1(u_{ov}, 0) = |O_{0,0}A(u_{ov}, 0) + O_{1,0}A(-u_{ov}, 0)|^2 \quad \text{Eq. (3.6)}$$

$$I_2(u_{ov}, 0) = |O_{0,0}A(u_{ov}, 0)e^{2\pi i u_{ov}} + O_{1,0}A(-u_{ov}, 0)e^{-2\pi i u_{ov}}|^2 \quad \text{Eq. (3.7)}$$

u_{ov} is the horizontal spatial coordinate of the middle point of the two diffraction spots and therefore, $I_1(u_{ov}, 0)$ represents the intensity of the overlap area in the first intensity measurement. $I_2(u_{ov}, 0)$ is the intensity of the area just mentioned, but in the second experiment with the tilted beam. The two intensities measured provide two equations out of four to solve for the amplitude and phase of $O_{n,m}$ if $A(u, v)$ is a known function. In fact, the aperture function would have the value of unity for all point in the absence of aberration. This would not be valid in presence of aberration and the function would have a phase change induced by aberration coefficients. In both cases, if there exist a model describing the aperture function, aperture function can be deconvolved from the

object transmission function to solve the phase equations. Therefore, aberrations are neglected here just to demonstrate that the equations are solvable if a good estimation of the aperture function exists. It would be addressed in the later sections of this chapter how this estimate is made and how iterative algorithms of phase reconstruction enhance this estimation by updating the guess of the probe in each iteration. The other two equations are the intensities of the beams in the non-overlap regions [13]:

$$I_1(0,0) = |O_{0,0}A(0,0)|^2 \quad Eq. (3.8)$$

$$I_1(u_0, 0) = |O_{0,0}A(u_0, 0)|^2 \quad Eq. (3.9)$$

Having equations 3.6 to 3.9 and assuming the aperture function is unity, we can solve for the phase and amplitude of the $O_{n,m}$ function which contains the phase and amplitude of the reciprocal lattice transmission function.

The same treatment can be expanded for multiple beams and multiple tilted-beam experiments to reduce the uncertainty of the phase equations. The goal is to link the object transmission function to the atomic potential of the material. As proposed in the literature [13, 14], the object transmission function's phase relates to the atomic potential via equation:

$$o(x, y) = Ae^{i\sigma \int V(x,y,z)dz} = Ae^{i\sigma V_t(x,y)} \quad Eq. (3.10)$$

A being the amplitude of the function, σ is a constant describing electron scattering power of the atoms. $V(x, y, z)$ is the potential of the crystal and $V_t(x, y)$ is the potential

function integrated on thickness of the crystal which is called the *Projected Atomic Potential*.

3.3 extended Ptychographical Iterative Engine (ePIE) Algorithm

A simple analytical solution to the phase problem was demonstrated in section 3.2. It is also possible to approach this problem with iterative methods. The first iterative method of phase retrieval was proposed by Gerchberg and Saxton in 1971 [13, 16]. This approach uses a random phase map for the object in the beginning step of the algorithm and updates the object by retrieving the phase information in the diffraction pattern via Fourier transforms. The effect of the probe convolution with the object is neglected or not explained in their paper. Although it is a valuable preliminary solution for the phase problem, a more complex solution is needed in order to account for the intricacies of the beam-sample interaction.

The ePIE algorithm starts from a speculation of the Object $O(r)$ and Probe $P(r)$ complex values. In STEM conditions, this object would be the 2D object transmission function and the probe would be the 2D complex valued function representing the localized electron beam on the object. A unity vector is selected as the initial guess of the object. The initial guess for the probe is an inverse Fourier transform of an aperture. This aperture is a circle of unity values in a zero matrix which is also called a *Support Function*. For having a better initial guess of the probe, a phase modulation term is multiplied to

the function to account for aberrations. The phase modulation due to aberrations would be [17]:

$$\chi(u) = \frac{2\pi}{\lambda} \Re \left[\sum_{i=1}^N \sum_{l=0}^{L(j)} \frac{C_{l+j-1, j-l}}{j+l} \lambda^{j+l} (u^*)^j u^l \right] \quad Eq. (3.11)$$

Parameters of Eq.3.11 are summarized in Table 3.1

Table 3.1 Parameters of Eq. 3.11 summarized

Parameter	Definition	Parameter	Definition
λ	De Broglie's wavelength of electron beam	$L(j)$	$\min(j, N - j)$
\Re	The real part of the polynomial	l	$1 \leq j + l \leq N$
N	Highest order of aberrations to be calculated	u and u^*	Complex angular coordinate u and its complex conjugate u^*

Hence, the probe function in reciprocal space would be:

$$P(u) = A(u)e^{-i\chi(u)} \quad Eq. (3.12)$$

which is basically the aperture function multiplied by aberration wave modulation.

Afterwards, for having the probe function in real space, an inverse Fourier transform is performed on $P(u)$ to derive $p(r)$ (see Appendix I). The object transmission function $o(r)$ will have a greater size in pixels to allow the shifting of the probe. As an initial guess, the complex unity vector or $1 + 1i$ is assigned to all pixels. Each pixel in the object, dx , has a specific length (in Å) that is derived from the length of the pixel in reciprocal space dK (in Å⁻¹). If the diffraction patterns collected are $N \times N$ pixels, the relationship between the pixels in real and reciprocal space is defined by Eq.3.13 [18]:

$$dx = \frac{1}{N \times dK} \quad Eq. (3.13)$$

Having recorded j diffraction patterns, each diffraction pattern is assumed to come from the j_{th} subset of $o(r)$. It is obvious that these subsets overlap since the illumination is redundant. Next step would be forming the first exit-wave out of the initial guesses of the object and the probe for the j_{th} subset of $o(r)$ [19, 20]:

$$\psi_j(r, R) = p(r - R_j) \cdot o(r) \quad Eq. (3.14)$$

$r = (x, y)$ in our previous notation and R_j is introduced into the equation to represent the shifting illumination. Referring to the fact that the recorded diffraction pattern ($I_j(u)$) is the amplitude squared of the Fraunhofer plane, the square root of the diffraction pattern is substituted with the amplitude of the Fourier transform of the guessed j_{th} exit-wave [20]:

$$\Psi_j(u) = \sqrt{I_j(u)} \frac{\mathcal{F}\{\psi_j(r)\}}{|\mathcal{F}\{\psi_j(r)\}|} \quad Eq. (3.15)$$

Then, this function is inversely Fourier transformed to yield [20]:

$$\psi'_j(r) = \mathcal{F}^{-1}\{\Psi_j(u)\} \quad Eq. (3.16)$$

Now $\psi'_j(r)$ constitutes the updated exit-wave for this iteration for the j_{th} subset. Straight away, the object and probe functions $o(r)$ and $p(r)$ are updated via Eq.3.14 and Eq.3.15 [18, 20]:

$$o_{j+1}(r) = o_j(r) + \alpha \frac{p^*(r - R_j)}{|p(r - R_j)|_{max}^2} (\psi'_j(r) - \psi_j(r)) \quad Eq. (3.17)$$

$$p_{j+1}(r - R_j) = p_j(r - R_j) + \beta \frac{o^*(r)}{|o(r)|_{max}^2} (\psi'_j(r) - \psi_j(r)) \quad Eq. (3.18)$$

α and β are the feedback parameters. The upper limit in the literature for these variables is suggested to be 1 and the lower limit varies between 0.1 [21] and 0.5 [16]. R_j is a matrix containing the spatial coordinates of the scanning grid. Since the scanning grid will not probably mesh well with the integer number of pixels, a fraction of the pixel length (dx) must be added to the shifting matrix R_j . In the paper discussing ePIE algorithm, the authors do not clarify if R_j contains these fractional values or not in the reconstruction software [20]. This concept will be further discussed in section 3.4.3.

Although both equations are updating the object and probe, their implementation does not happen at the same time. Usually, updating the probe begins after several full iterations of the ePIE algorithm. The reason is that the guess of the probe is closer to the actual probe compared to the guess of the object (unity complex vector). Updating the probe is postponed until a good estimate of the object is made.

Once the update is completed for all j diffraction patterns, one iteration of the ePIE algorithm is completed. The error metric for a non-simulated case where the original $o(r)$ is not accessible, would be a comparison of the Fourier transform of each subset of the reconstructed object with its corresponding diffraction pattern. Eq.3.19 is the definition of this error metric [20].

$$E_{\Psi} = \frac{\sum_j \sum_u |\sqrt{I_j(u)} - |\Psi_j(u)||^2}{\sum_j \sum_u I_j(u)} \quad Eq. (3.19)$$

It is worth to note that after application of the probe update, convergence of the algorithm accelerates.

3.4 Other Phase Retrieval Algorithms

3.4.1 Wigner Distribution Deconvolution

As mentioned earlier, the amplitude of the diffracted wave can be modeled by the Fourier transform of the exit-wave as a function of reciprocal-space coordinates u and probe positions R in Eq. 3.20 [22].

$$M(u, R) = \int a(r - R) o(r) e^{2\pi i r \cdot u} dr \quad Eq. (3.20)$$

$a(r - R)$ being the aperture function in real space and $o(r)$ being the object transfer function. The amplitude squared recorded by the CCD can be reformulated as Eq. 3.21 due to the convolution theorem in Fourier transform as [22]:

$$|M(u, R)|^2 = \iint A(b') A^*(c') O(u - b') O^*(u - c') e^{2\pi i R \cdot (b' - c')} db' dc' \quad Eq. (3.21)$$

b' and c' being the integral dummy variables. $A(b')$ and $A^*(c')$ are the complex conjugated Fourier transform of the aperture function. Similarly, $O(u - b')$ and $O^*(u - c')$ are the complex conjugate of the Fourier transform of the object transfer function. By taking the forward Fourier transform of $M(u, R)$ with respect to the probe positions R and backward Fourier transform with respect to u , a function is created that

allows separation of the variables belonging to probe and sample. This will allow to deconvolve the effects of the probe phase from the exit wave, calculating the object transfer function phase. This function is shown in Eq. 3.22 [22].

$$H(r, R') = \int a * (b)a(b + r)e^{-2\pi i R' b} db \int o * (c)o(c + r)e^{2\pi i R' c} dc \quad Eq. (3.22)$$

$$H(r, R') = \chi_a(r, -R')\chi_o(r, R') \quad Eq. (3.23)$$

As represented in Eq. 3.22, $H(r, R')$ has two components: $\chi_a(r, -R')$ and $\chi_o(r, R')$, that are purely a function of the probe and object. Thus, by multiplying the complex conjugate of the probe related term into $H(r, R')$ and dividing the result by the amplitude squared of it, the effect of the probe is deconvolved. A small quantity ϵ is added to the amplitude squared to avoid division to zero as shown in Eq. 3.23 [22].

$$\chi_o(r, R') = \chi_a^*(r, -R')H(r, R')/(|\chi_a(r, -R')|^2 + \epsilon) \quad Eq. (3.24)$$

While the specimen related term is calculated by Eq. 3.23, the specimen function $o(r)$ need to be solved for. This solution is carried out more easily by taking the Fourier transform of $\chi_o(r, R')$ with respect to r [22].

$$D(u, R') = O(u)O * (u - R') \quad Eq. (3.25)$$

The finite aperture size imposes a frequency limit in R' direction; meaning that there is a maximum frequency that is transferred by the aperture function and higher frequencies are suppressed. Therefore, for calculating $\chi_o(r)$ that contains the phase information of the sample, $O(u - R')$ shall be multiplied by $D(u, R')$ and be divided

by its amplitude squared for all existing values of R' below the maximum cut-off frequency to yield $O(u)$. Afterwards, it is possible to take the back Fourier transform of $O(u)$ to compute the $o(r)$ as represented in Eq. 3.25 [23].

$$O(u) = \frac{\sum_{R'} O(u - R') D(u, R')}{\sum_{R'} |O(u, R')|^2} \quad |R'| \leq R'_{max} \quad Eq.(3.26)$$

Here, the effect of the probe complex function was deconvolved from the exit-wave and object transmission function is calculated. Wigner Distribution Deconvolution (WDD) uses the areas of the diffraction pattern containing signal and hence, is less susceptible to noise [24]. This deconvolution has an advantage over the iterative engines and that is the analytical solution to the phase problem which is both more deterministic and faster in terms of implementation. The drawback would be that this solution requires a good guess of the probe function. A support function, which is basically a matrix of zeros surrounding a circle of ones, is used as the aperture function and is back Fourier transformed to give the probe function. It is true that this is not identical to the aperture function of the microscope due to the fact that the aperture is not a perfect circle (it may be dirty!) and non-precisely measurable aberrations exist in the probe wave front. Hence, an algorithm such as ePIE that is adapting the probe function more to the reality of the experimental value based on the information embedded in the diffraction patterns, has the advantage over this analytical method.

3.4.2 Ptychographical Iterative Engine PIE

The PIE algorithm is the older version of the ePIE algorithm described in section 3.3. It is similar to this algorithm in many ways, except several aspects. The probe function is not updated throughout the algorithm in contrast to the ePIE (the “e” prefix before “PIE” is referring to the updating of the probe). Instead, the initial guess of the probe should be accurate enough and adjusted in the object update equation as shown in Eq.3.27 [19].

$$o_{j+1}(r) = o_j(r) + \beta \frac{|p(r-R)|p^*(r-R)}{|p_{\max}(r-R)|(|p(r-R)|^2 + \alpha)} (\psi'_j(r) - \psi_j(r)) \quad Eq. (3.27)$$

α is for preventing division by zero and β is the feedback parameter for the update function. $\frac{|p(r-R)|}{|p_{\max}(r-R)|}$ is normalizing the difference in each step, maximizing the influence of update for pixels within the bright region of the probe. When the complex conjugate of the probe function, $p^*(r-R)$, is multiplied to the exit-wave difference, the effect of the phase of the probe is negated, and its amplitude squared remains in the function. Hence, the function is divided by $(|p(r-R)|^2 + \alpha)$ to fully cancel out the probe from the exit-wave difference to be added to the previous estimate of the object.

The overlapping of the illumination scanning positions plays a key role in the quality and uniqueness of final the final reconstructed image. The overlap measure is defined as [25]:

$$o = \left(1 - \frac{a}{2r}\right) \times 100\% \quad \text{Eq. (3.28)}$$

o being the overlap percentage, a the center-to-center separation of the illumination circles and $2r$ being the diameter of the circles. This measure of overlap is not considering the overlapping area of illumination, but only the 1D displacement of the probe. An overlap of more than 60% has been advised by literature for having a “high quality” Ptychographical reconstruction [25].

3.4.3 Super-Resolution extended Ptychographical Iterative Engine SR-ePIE

The Super-Resolution ePIE algorithm is a more recent version of the ePIE algorithm introduced by Maiden et al. [18]. This algorithm does not differ in core characteristics with the ePIE algorithm which are Fourier transform based analysis, substituting the diffraction amplitude with the amplitude of the exit wave and updating both the object and probe functions. However, it has four major differences with its predecessor as listed in the following bullet points and related explanations:

- Creating estimations of the diffraction patterns

The length of a pixel in real space (dx) is linked to the maximum range of angles collected in reciprocal space. The wider the angular range of diffraction pattern, the smaller the dx would be. Recording larger area of the diffraction space could be equivalently explained as recording higher spatial frequencies that will eventually contribute to the final reconstruction. Since the size of the CCD recording the diffraction

patterns is finite, this is only possible by changing the *Camera Length* of the projection lenses. By reducing the camera length, higher angles in diffraction space fall upon the CCD. But the inherent problem in this approach is that the high intensity of the direct beam would eventually saturate the CCD pixels if it is defined by fewer and fewer pixels at some point. The consequence is that with the current dynamic range of the detectors, there is a limit on the maximum angle range that a CCD can record information within.

To numerically overcome the angular limit, SR-ePIE suggests to extrapolate the diffraction space. After several iteration of the ePIE algorithm is completed and a realistic guess of the object and probe are made, both object and probe functions are up-sampled by a factor $c > 1$ by bicubic interpolation. Therefore, the exit-wave's Fourier transform $\Psi_j(u)$, which later its amplitude is going to be substituted with the square root of the diffraction patterns recorded, will also have c times more pixels in x and y directions compared to the original functions. Hence, for amplitude substitution to be possible, only the amplitude of the central $N \times M$ pixels of $\Psi_j(u)$ which is of $cN \times cM$ pixels would be replaced. The amplitude is only replaced in the central $N \times M$ pixels and the higher frequencies are calculated based on the previous guesses of the object and probe. Hence, the higher q -space (diffraction space) information are estimated based on the Fourier transform of the up-sampled exit-wave. This will create a "virtual detector" c times larger than the original detector. An improvement of resolution in experimental cases is shown in their work via computer simulations [18].

- Subpixel Shifting of the probe

As introduced in 3.4.2, the positions of scanning points do not fall within integer multiples of dx . Therefore, a fraction of dx 's length should be added to the matrix defining the scan positions, i.e. R_j . This is a shift that has a value less than a length of a pixel, and that is the reason it is called a *Subpixel Shift*. While subpixel shifting is not easily feasible in real space, it is easily done in reciprocal space by multiplying a phase ramp into the probe [18]. This concept that a shift in real space is equivalent to applying a phase ramp in reciprocal space was also introduced in section 3.2. The exponent of this phase ramp would be subpixel fraction of dx and the phase ramp is applied to the probe function before multiplying it with the object's j_{th} subset.

For the next diffraction pattern, or the $j + 1_{th}$ subset of the object, the probe should be subpixel shifted back to its initial position corresponding to zero subpixel shift. This is similarly done by applying the negative phase ramp equal to the first ramp [20]. The computation cost could be lowered by merging this step with subpixel shifting the probe for the $j + 2_{th}$ step. In other words, two phase ramps could be applied at the same time by adding them in the exponent of the exponential:

$$Total\ phase\ ramp = e^{-i\varphi_{j+1}(u)+i\varphi_{j+2}(u)} \quad Eq. (3.29)$$

As will be discussed in chapter 5, the exact definition of position of the scanning grid for the reconstruction software is crucial. In fact, due to systematic errors in data acquisition such as drift and unsystematic or random errors such as inaccuracies of

positioning of the scanning unit of the microscope, the final reconstruction is entirely degraded. If a systematic error as the subpixel positioning error is introduced in addition, the results would further degrade. In fact, the PIE algorithm may diverge if subpixel shifting is not incorporated as shown in Figure 5 of reference [18].

- Overlap or redundancy measure introduced

A measure of redundancy in data collection is put forward as follows [18]:

$$\sigma_{PTY} = \frac{\text{Total \# of Pixels in 4D diffraction Dataset}}{2(\text{\# of pixels in } o(r) + \text{\# of pixels in } p(r))} \quad \text{Eq. (3.30)}$$

This ratio represents the same concept introduced in section 3.2 about the number of known variables versus unknown parameters. The numerator of the above fraction represents the number of measured values or known parameters of the equation systems. The denominator, on the other hand, is the number of unknown parameters of the equations which are the complex values of $o(r)$ and $p(r)$. The number 2 before the parentheses is due to the fact that both probe and object transmission functions are complex valued and both the real and imaginary parts of these functions should be computed. If $\sigma_{PTY} > 1$, the Ptychographical reconstruction problem is considered to be well-conditioned [18]. This criterion for redundancy seems to be more promising since in the previous benchmark explained in section 3.4.2, an accurate definition of the radius of the practical STEM probe on the sample is needed. This measurement would be an onerous task due to many complexities involved such as the Detector Quantum Efficiency (DQE), *Modulation Transfer Function (MTF)* of the CCD [26], aberrations of the imaging

lens system, pixelated measurement of the probe, etc. In addition, although this redundancy measure is not explained in previous papers discussing PIE and ePIE [20, 19], it should be applicable to these algorithms as well, for it is a generic mathematical expression of the linear system of equations.

- High frequency information suppression

High spatial frequency information suppression is carried out by adding a speckle to the outer region of the virtual detector. This speckle gradually brings the values of pixels in the outer region of the virtual detector to zero. This would make a more realistic virtual diffraction pattern in which the high frequency information has lower intensity. The convergence of this algorithm is enhanced compared to ePIE as reported by authors of this reference, although the authors do not specify the function that is executing this gradual decay of pixel values at higher angles [18].

3.5 Pros and Cons of Electron Ptychography

In this section, pros and cons of the electron Ptychography are addressed and the applications of it are discussed.

Since the signal intensity loss for a thin sample is negligible, the amplitude of the wave function can be presumed to be almost unchanged. The phase on the other hand, is sometimes severely change by atoms. Regarding the multiplicative model of interaction of the probe and specimen, phase changes more than 2π may be induced on the incoming

electron wave and thus, the weak phase object approximation is not fully correct. The assumption which should be held true is that the sample is thin [13] to minimize the effect of factors such as dynamic diffraction and inelastic scattering that are not taken into account in the mathematical model used by Ptychography. It can be generally assumed that the phase of the wave is more susceptible to change by a light atom than its amplitude and hence, it is more “sensitive” to light atoms. The observation of light atoms has been proven experimentally possible with Electron Ptychography as reports here.

H Yang et al. [27, 28] have shown the possibility of detecting Nitrogen and Oxygen atomic columns in GaN and the antiphase grain boundary of Ti, Nd doped BiFeO₃. A comparison to the ADF, ABF, Negative Spherical Aberration Imaging (NCSI) and WDD Ptychographical phase reconstructions are also demonstrated in their papers as reprinted in Figure 3.4.

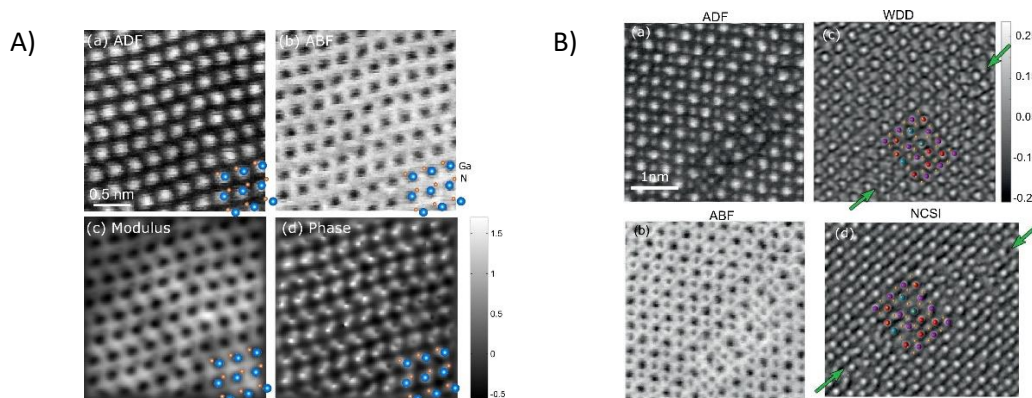


Figure 3.4 A) ADF, synthetic ABF, NCSI and WDD Ptychographical phase reconstruction of the antiphase grain boundary in Ti, Nd doped BiFeO₃. The oxygen column locations are marked with small yellow spheres. B) ADF, ABF, Modulus and phase of WDD Ptychographical reconstruction in GaN sample [28].

The Nitrogen atomic columns show distinguishable contrast in the WDD Ptychographical phase reconstructed, as opposed to invisible contrast in the HAADF and ABF signals in Figure 3.4.A. It is to be noted that the ABF technique has shown to reveal the lighter atoms such as Nitrogen, Oxygen and Hydrogen in crystals [29, 9], but the experimental conditions of Yang et al. papers under discussion have not been optimized for visualization of lighter atomic columns via ABF. While figure 3.4.B also shows the Oxygen lattice sites as yellow circles, the contrast in the Ptychographical reconstruction image is not making these columns clearly visible compared to the ABF signal according to author of this thesis.

Although the ABF datasets from which a synthetic ABF images are made in Figure 3.4 are not optimized specifically for the ABF experiment and the comparison between the two methods are not based on fair grounds, there are several advantages for having a Ptychography dataset over the sole ABF. First, the ABF, or generally all the STEM signals, can be later reconstructed by acquiring a 4D dataset of diffraction patterns since the whole diffraction field is collected. This could be done by defining a digital virtual (annular) detector in the collected diffraction field. It should be noted that for having a good quality synthetic image, the conditions of that specific experiment should be adjusted prior to diffraction pattern collection. For example, for having a favorable HAADF signal, the beam should be meticulously focused on the sample. Else, the desired quality of the synthetic image will not be achieved after 4D dataset collection with non-optimal experimental conditions. Second, Ptychography has shown to have less sensitivity to defocus and,

generally, aberration conditions of the probe compared to the other well-established STEM techniques because of its inherent principle of deconvolving the probe function. In other words, the complex probe function is deconvolved from the object transmission function and ideally, the image is freed from the aberrations of the probe. Atomic resolution Electron Ptychography can be accomplished with a defocus of as high as 80 nm as shown by Song et al. [30]. The advantage lies in that it is not a firm requirement of a Ptychography experiment to fine-tune the probe before the experiment since, whatever are the conditions of the illumination function, it will be deconvolved at the end; except the redundancy of the data collection shall remain intact.

Given that this deconvolution ideally negates the effect of aberrations, Ptychography is expected to have a better spatial resolution. Several cases of gain in resolution has been demonstrated in the literature. Yang et al. showed the gain in resolution by Ptychography on detecting Fullerene spheres inside a Carbon nanotube (CNT). While the contrast in the ADF signal is only showing the single Iodine atoms, phase reconstruction via WDD shows the Fullerene inside the nanotubes as shown in Figure 3.5.A [24]. The authors have also shown the gain in resolution by Fourier transform of WDD phase reconstructed structure of a Gold nanoparticle. Although an increase in intensity is visible for higher frequencies in the Fourier space, the effect only can be regarded as an improvement to a confined extent.

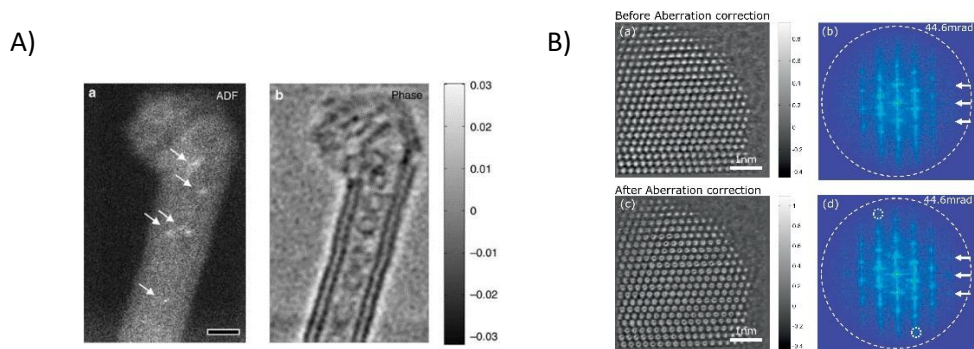


Figure 3.5 A) visualization of Fullerene inside CNT and B) resolution improvement via Ptychography shown in Gold nanoparticles.

Another improvement of resolution is shown by Jiang et al. on mono- and double-layer of Molybdenum di-Sulfide (MoS_2) [21]. The resolution achieved by this work using ePIE Ptychography is 0.4 \AA which is better than the resolution achieved by standard STEM imaging methods with similar experimental conditions. They have reached the information limit of 5α (α being the convergence semi-angle of the probe) in Fourier space which is more than twice the limit of resolution achieved by ADF (2α). Also shown in their work, is the ePIE reconstruction of a bi-layer of MoS_2 with relative rotations of 6.8° between the two sheets. This rotation creates a *Moiré Pattern*. This sample serves as a benchmark for resolution since the distances between intensity peaks in the projected image could possess a wide range of values. The minimum detectable distance in phase reconstruction image has been reported to be 0.4 \AA in this experiment.

In this paper, it can be noticed that there is an inconsistency with respect to the theory of resolution which should be addressed here. The calculation of Rayleigh limit of resolution, discussed in section 2.2 of this thesis, seems to be inconsistent with the definition of Rayleigh scattering in their work [21]. The Rayleigh resolution criterion states

that the minimum resolvable distance in a diffraction limited (r) system would be $0.61\lambda/\alpha$, λ being the wavelength of the illumination and α the maximum semi-angle within which diffraction information exists [31]. Due to this criterion and the experimental information that they have reported (80 KeV, 2α limit for ADF STEM), the Rayleigh limit of resolution for STEM conditions would be:

$$r = 0.61 \frac{4.17 \times 10^{-12} \text{ m}}{2 * 21.4 \text{ mrad}} = 0.59 \text{ \AA}$$

which is in contrast with what they have calculated under the caption of the Figure 3. in the paper (1.2 Å). Furthermore, the Abbe resolution, which is essentially a less strict condition for measuring resolution, is defined by [31]:

$$\textit{parallel illumination} : r = \frac{\lambda}{\textit{Numerical Aperture}(\sin(\alpha))} \quad \textit{Eq. (3.30)}$$

$$\textit{oblique illumination} : r = \frac{\lambda}{2 \times \textit{Numerical Aperture}(\sin(\alpha))} \quad \textit{Eq. (3.30)}$$

Since the illumination is non-parallel in STEM, the diffracted beam that is not allowed in parallel illumination condition in the diffraction pattern, is allowed in the diffraction pattern by the numerical aperture because of using a big convergence angle. Therefore, the Abbe's resolution for STEM conditions would be the oblique illumination criterion. Based on this, for the Ptychographical reconstruction conditions Jiang et al. have reported (5α , 80 KeV), and the Abbe's resolution limit would be:

$$r = \frac{4.17 \times 10^{-12} \text{ m}}{2 \times \sin(5 \times 21.4 \text{ mrad})} = 0.19 \text{ \AA}$$

Which is also in contrast to what is reported as Abbe's resolution in the abstract and throughout the paper (0.39 Å) [21]. In addition, by stating that the reconstruction image has reached Abbe's resolution, the implication is that the only factor limiting the resolution is the physical limit of diffraction. This means the reconstructed image is totally insensitive to mechanical and thermal noise in the microscope, point spread function of the CCD and the aberrations of the probe. In contrast, as shown in the discussion before, the reconstruction in this work is not reaching Abbe's resolution limit, but approximately twice this limit. Accrediting that Electron Ptychography is a powerful technique because of using a bigger numerical aperture and negation of aberrations by deconvolution of the probe from the object, reaching the limit of resolution which is physically imposed by diffraction phenomenon remains challenging in experiment.

As shown in [32], there is a certain thickness below which the effect of beam propagation could be neglected and the sample could be regarded as a projected potential. This thickness depends on the wavelength of the probing wave and the convergence semi-angle of the illumination. Since both samples used in [21] are of utmost practical thinness (a 2D material), the electron wave propagation and diffuse scattering is minimized. The thickness is still more than the amount less than which the effect of beam propagation could be neglected as stated by the authors of [32]. Moreover, contrast interpretation would be much more robust due to thinness of the samples since the *Phase*

Wrap phenomenon does not happen (see section 4.3). While Ptychographical phase reconstruction for MoS₂ monolayers is accomplished with success, the application of this technique on practical real samples prepared for TEM analysis (typically ~50-100 nm) remains challenging.

For having the optimal experimental conditions in ABF, ADF or similar signals, time should be spent on focusing or correcting the probe conditions to yield the best results. Attaining ideal conditions for regular STEM imaging will require to introduce extra electron dose on the sample and this would be critical for beam-sensitive materials. The effect of electron dose has been studied in several works. Jiang et al. [21] showed the ptychography resolution is limited by the convergence semi-angle of the probe if the dose is high ($>10^4$ e/ \AA^2) and *Poisson Noise* limited for lower dose. They have also studied the effect of electron dose on WDD and ePIE Ptychography reconstruction quality [21]. Humphry et al. [33] have achieved an atomically resolved image of gold nanoparticles in a modified Scanning Electron Microscope (SEM). They have placed a CCD camera after the sample and collected the diffraction patterns in an experimental setting quite similar to STEM. The advantage of their work is using a low acceleration voltage (30 KeV), which reduced the electron beam damage. In addition, the electron dose also used by them is an order of magnitude lower than what has been reported in STEM Ptychography literature (3.3×10^3 e/ \AA^2). Consequently, the resolution achieved is also lower (2.3 \AA). Pelz et al. [34] have shown via simulations that, in principle, using a dose 100 times lower than what was used by Humphry et al., it is possible to perform Ptychographical reconstruction

on biological macromolecules. Their approach would allow these beam-sensitive molecules to be included in the materials that can be characterized with electron Ptychography. The issue of electron dose gains higher importance when the redundancy of the Ptychographical dataset is a precondition.

Chapter 4: Innovative Approaches to Ptychography

4.1 The concept of Moiré-Ptychography

The regular atomic resolution in STEM imaging is based on collection of a periodic sampling signal. The most commonly used periodicity is a rectilinear pattern of points which is called the *Scanning Grid*. This scanning grid can be described by a sampling wave having a certain spatial frequency. In case the sample under study is crystalline, as shown in chapter 3, it could also be described as a wave with its frequency being determined by the d-spacing of the crystal in different direction. With this consideration, the sampling wave is interfering with the crystal wave and the signal collected (e.g. HAADF) is an interference pattern. The frequency of the sampling wave used in conventional STEM imaging is higher than the spatial frequency of the crystal lattice. This means that the distance between scanning points in the scanning grid is smaller than the distance of atoms and the probe is *Oversampling* the periodicity of the crystal. If the sampling wave's frequency is close to or lower than the lattice, it is *Undersampling* the lattice wave. Undersampling creates an interference pattern similar to the *Moiré Patterns* or *Moiré Fringes* in TEM terminology.

In spite of what may seem counter-intuitive, the undersampled signal carries a great wealth of information. In STEM specifically, undersampled HAADF signal has been used to make atomic resolution lattice images at lower magnifications than that is needed for atomic resolution imaging (e.g. 100x-1Mx) [35], study of dislocations in crystal interfaces [35], and measuring strain fields in crystals [36]. Undersampled STEM, although

may only be applicable to crystalline materials, has several advantages. Firstly, the signal covers a great field of view and the long-range order of the matter can be probed. Secondly, it has basically the same geometrical information as an oversampled signal without loss of information in many cases. Thirdly, distribution of the electron dose due to longer scanning leaps, reduces the dose exposed to the sample and this would be extremely beneficial for beam-sensitive crystalline samples.

The idea of *Moiré-Ptychography* attempts to apply the concept of retrieving information from an undersampled signal to Ptychography and take benefit of undersampling in this context. The idea is to collect 4D dataset of diffraction patterns from a 2D scanning grid that has a step size close to or larger than the lattice constants to retrieve the phase of the transmission function. In other words, the signal is undersampled in real space (and not the reciprocal space). This is ostensibly contradicting the redundancy principle of Ptychography. Following the explanation provided in chapter 3, the Ptychography dataset collected should be redundant in real space to ensure that there is a unique solution for the phase problem and the phase information is fully reserved and reflected in the diffraction dataset collected. If the scanning points are farther apart than the diameter of the electron probe, then the beam does not overlap itself in the scanning grid and the redundancy is lost. If the assumptions that the crystal is periodic and the thickness of the specimen is constant are made, it could be argued that the CBED pattern collected from a certain location on the lattice is equivalent to the diffraction pattern collected from the same relative position from any unit cell. For a

better explanation, Figure 4.1 is provided. Figure 4.1.A shows the projected potential of Silicon crystal in [100] zone axis for four Si columns, or the 2D unit cell. On this projected potential image, five positions of the electron probe in each of x and y directions are shown, adding up to total twenty-five scan positions. Therefore, the distance between the two adjacent atomic columns in x and y directions are probed with five scanning points with overlap of 50%. In order to collect the same diffraction patterns with Moiré-Ptychography, the same twenty-five diffraction patterns must be collected from five unit cells as shown in Figure 4.1.B. If the distance between the adjacent Si columns in x and y crystal directions is d_c and the scanning step size in conventional Ptychography is d_s , then the scanning step size in Moiré-Ptychography would be $d_s + d_c$. Although the probe positions do not overlap physically while the Moiré-Ptychography dataset is collected, the redundancy is assured in reconstruction stage by defining the system of coordinates for the reconstruction software based on only d_s . In other words, the software is not “aware” of the real scanning step size ($d_s + d_c$) and receives the 4D dataset as if it were a normal Ptychography dataset acquired with d_s scanning step size.

By doing so, the area which has been exposed to electron current has increased by a factor of 25, implying that the electron dose is reduced by a factor of 25. In fact, by increasing the overlap percentage necessary in Moiré-Ptychography, the dose would be further reduced, which is entirely counter-intuitive and opposite to the normal Ptychography setting! Since the dose is further reduced with increasing the overlap

percentage, high redundancy of the data collection is assured which will help providing a unique solution to the phase problem and increase the signal to noise ratio.

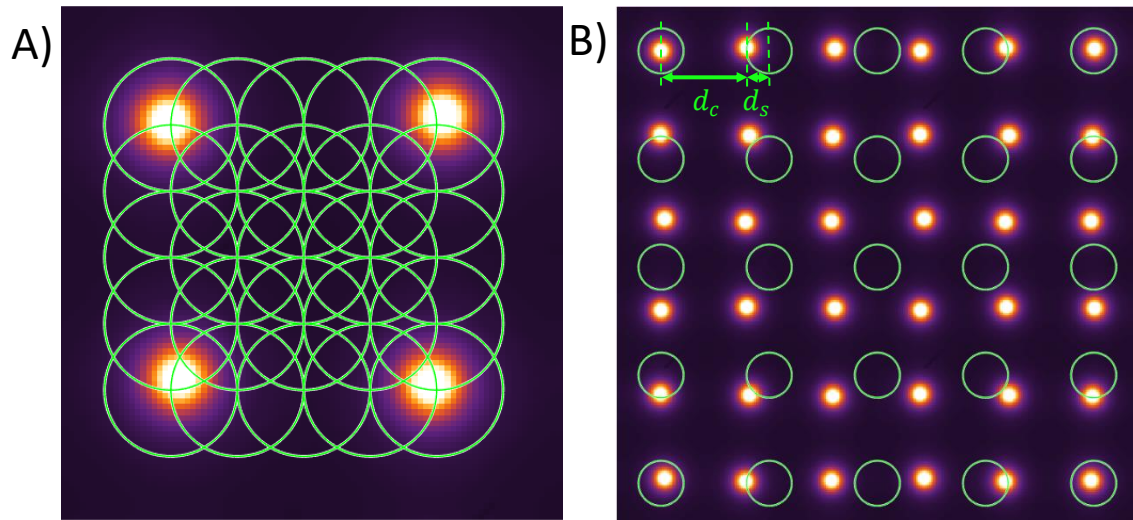


Figure 4.1. A) Ptychography scanning positions shown on the projected potential map of a Si crystal in [001] zone axis. Green circles denote the electron probe. B) Equivalent dataset in A) acquired with Moiré-Ptychography

The example shown in Figure 4.1 is a demonstration of a straightforward case since the scanning grid and the Silicon FCC crystal projection in [100] are both of rectilinear geometry and are not rotated compared to each other. Therefore, the 4D array of the diffraction patterns does not need to be reshaped and only by adjusting the scanning step size in the software, the reconstruction would be accomplished.

To see it from a different perspective, the ordering of the diffraction patterns remains intact. In practice, the experiment would not necessarily have the same conditions. When the crystal's projection in a certain zone axis does not have the same 2D lattice parameters (d_c) in x and y, $d_s + d_c$ will not probe these directions similarly. As

illustrated in Figure 4.2.A, if $O_{0,0}$ is the first scanning point, $(O_{1,0}, O_{2,0}, \dots)$ are probing the x direction and $(O_{0,1}, O_{0,2}, \dots)$ are probing the y direction. It is evident from this figure that with the chosen step size, each scanning point in x direction is moving in increments with respect to the previous point and ultimately reaching a point equivalent to $O_{0,0}$. Re-ordering the diffraction patterns is not needed in this case. On the contrary, the probe in y direction does not raster sequentially with regards to the unit cell. As an example, $O_{0,1}$ is scanning a point farther from $O_{0,0}$ compared to $O_{0,2}$ in the unit cell. This creates a problem of indexing diffraction patterns and the 4D diffraction patterns need to be reshaped for the reconstruction to be meaningful. Generally, the indexing problem exists when the zone axis pattern does not have the same symmetry as the scanning grid (Figure 4.2.A), or the scanning grid is rotated in crystal coordinates system (Figure 4.2.B).

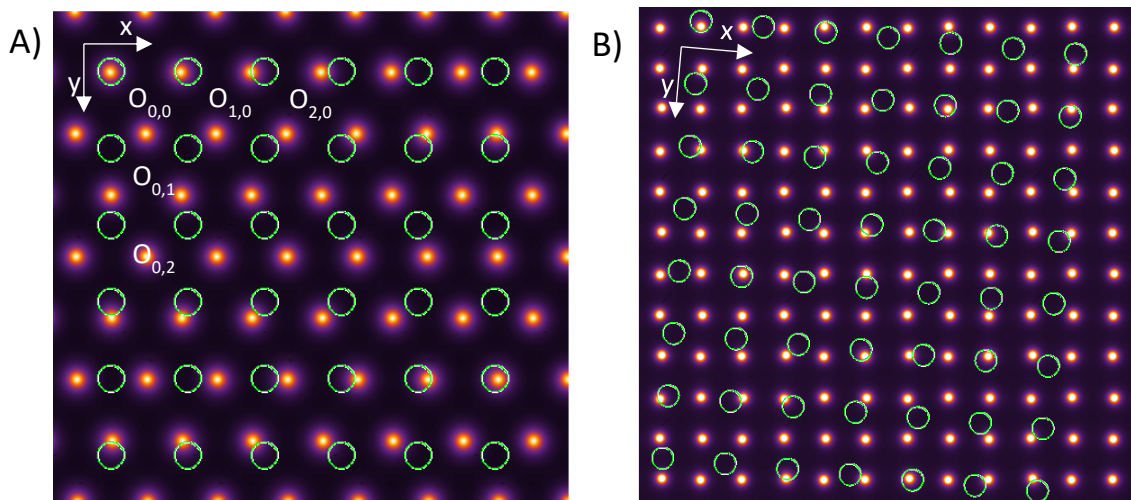


Figure 4.2. Demonstrating the indexing issue when A) crystal projection and the scanning grid do not have the same symmetry type (6-fold vs 4-fold) and B) the scanning grid's (x,y) base is rotated compared to the crystal

To overcome the indexing problem, two strategies can be taken. The first one would be to change the base of the scanning grid in a way that follows the crystal symmetry. For example, if the crystal projection is a parallelogram, the scanning grid should be a rescaled parallelogram with the same angles for the re-indexing to be unnecessary. This option may not be feasible for the current software controlling the scanning unit in TEM. The second would be keeping the same equispaced and orthogonal scanning points and then reshaping the 4D array of diffraction patterns. An idea has been developed for the second approach.

If the crystal projection is regarded as a 2D recurring unit cell, a base is defined by the crystal unit cell that is expressed by the 2x2 matrix C . Each scanning point in the grid can be regarded as a vector and the whole scanning grid can be expressed as a nx2 matrix S . The rotation of the scanning grid relative to the crystal base is inherent in the S matrix and there is no need to add another transformation to calculations. In order to change the base to an orthonormal basis (2x2 unity I), a transformation matrix M is defined as:

$$M = I \times C^{-1} = C^{-1} \quad Eq. (4.1)$$

In order to express the scanning grid in crystal's basis, the transformation matrix M is applied on it to yield $S \times M$. In order to calculate the positions of the scanning points with regards to the system of coordinates defined by the unit cell of the 2D crystal, the operator $R_t[]$ is defined as if it applies on a matrix, the result would be the remnants of

a division to t for all of the elements of a matrix inside brackets. Now the *Matrix of Remnants* is calculated in the orthonormal base by calculating $R_1[S \times M]$. Finally, the new Moiré-Ptychography scanning grid S_{MP} that is to be fed into the Ptychography algorithm would be defined as:

$$S_{MP} = R_1[S \times C^{-1}] \times C \quad Eq. (4.2)$$

S_{MP} is a matrix containing the information of relative positions in the unit cell the probe has scanned. This matrix is given to the ePIE instead of the scanning grid consisting of squares to define the system of coordinates.

In order to have a better grasp of what exactly the Moiré-Ptychography re-ordering is doing, using the analogy of “transparent tiles” for describing would help. In this analogy, the unit cells of the 2D crystal can be seen as transparent tiles. Therefore, the 2D crystal would be a surface created by attaching these tiles to each other. One can imagine that the scanning process leaves a “stain” on the scanned location on each tile. The effect of the transformation matrix is to reshape the tiles to be squares. In other words, the 2D crystal is brought into the orthonormal space. After applying the transformation matrix, the “tiles” are of orthogonal unity sides and “stains” pattern has also moved accordingly because the tiles have been deformed. The process of calculating the relative positions of scanning points in the unit cell can be viewed as if the transparent tiles are detached and stacked on top of each other. If the stack of

transparent tiles is now viewed from the top, the stains (or scanning positions) create a pattern. The pattern that the “stains” make is the S_{MP} matrix described earlier.

In each of the four image pairs shown in Figure 4.3, the left side shows the scanning grid (S) which is assumed to be lying on a 2D cubic crystal (invisible in the image) with different orientations, number of scanning points and scanning step sizes. The right side, on the other hand, shows the matrix of remnants which is calculated by applying $R_1[]$ on the scanning grid S .

As seen in Figure 4.3, the sampling of the specimen after moiré effect can have a non-uniform shape. 4.3.A shows a 30x30 grid with 1.4 unit cell step size and 25° rotation. The moiré remnants shown on the right side show a high percentage of overlap in one unit cell. 4.3.B shows a 10x10 grid with 1.2 unit cell step size rotated by 88°. As can be seen, the overlap percentage is not uniform throughout the cell. The advantage of the code developed for having these images is that the experiment can be designed before by trying different scanning parameters and finding out what settings gives a uniform redundant scanning. 4.3.C shows a 20x20 grid with 1.1 unit cell side step size only rotated by 1°. This would suffice for the grid to cover all the surface area of the unit cell after scanning 20 unit cells with 1° rotation. Figure 4.3.D is showing 40x40 scanning points with the step size identical to the unit cell side and zero rotation. In fact, the grid is always scanning the same equivalent point in the unit cell (vertices in this case). Therefore, the Moiré remnant shows that in relative unit cell system of

coordinates, all of the scanning point in the grid are equivalent and only shows one point at (0,0).

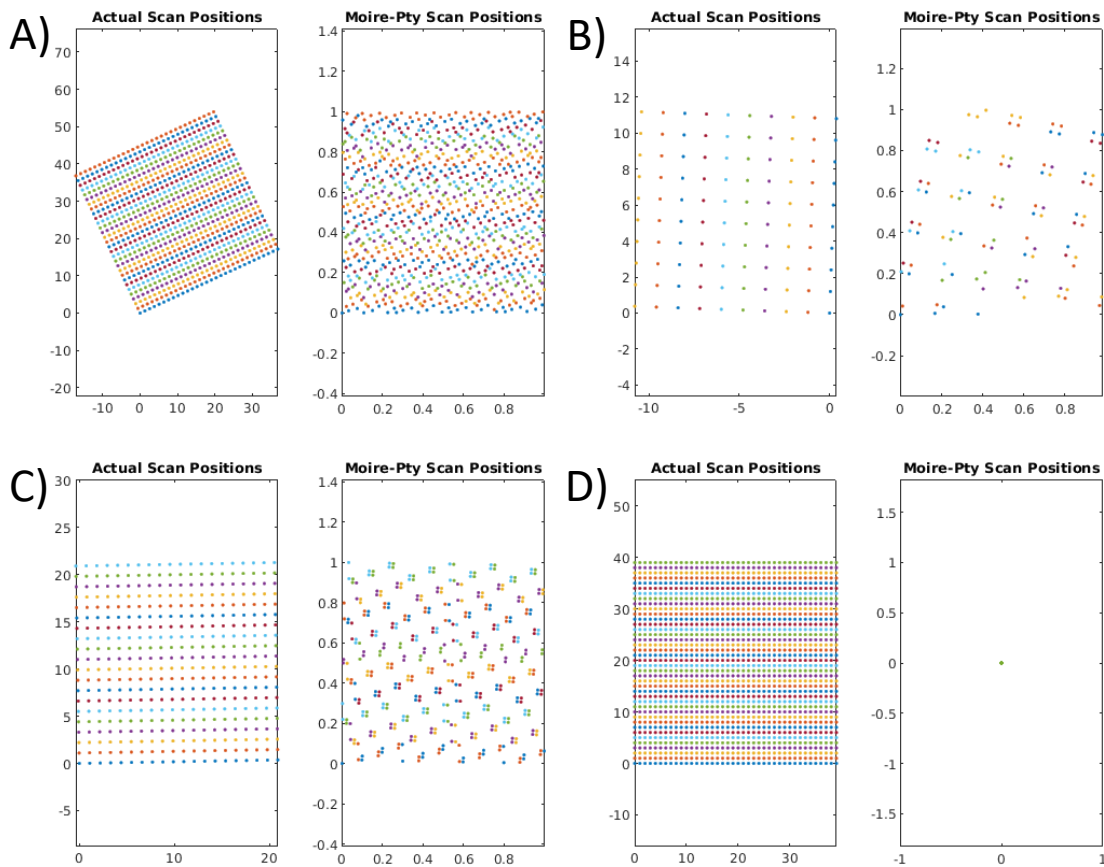


Figure 4.3. A) a $30 \times 30 \times 1.4 \times 25^\circ$ B) a $10 \times 10 \times 1.2 \times 88^\circ$ C) a $20 \times 20 \times 1.1 \times 1^\circ$ and D) a $40 \times 40 \times 1 \times 0^\circ$ scanning grid. Scanning grid on the orthonormal bases is shown on the left and the Moiré-Ptychography equivalent points is shown on the right of each figure.

4.2 Energy Filtering of the CBED Patterns

As discussed in section 2.5, beam-specimen interactions fall into several categories. Among all, the elastic and inelastic interactions are the most important interactions in forward scattered electron. In a perfect thin crystal under the TEM beam,

if the inelastic scattering is neglected, the elastically scattered electrons constitute the diffraction plane as a grating of sharp peaks of intensities. These electrons are diffracted by different crystal planes in Bragg angles with negligible or no loss of energy. If the illumination is perfectly parallel, the diffraction spots appear as infinitesimally small dots and if convergent, as perfect circles (neglecting the effect of aberrations and CCD). As the thickness of the samples increases, the relative intensities between diffracted spots varies due to the dynamical diffraction effects. Moreover, some of the elastically scattered electrons experience inelastic interactions in their path due to higher probability of inelastic scattering in a thicker sample. Inelastically scattered electrons also experience elastic interactions on their path and can contribute to the intensity of the diffraction spots, but, with an incoherent phase. . Therefore, it is expected that a portion of electrons in all the Bragg diffracted beams also experience or have had experienced inelastic collisions, as well as the direct beam. The probability of having an inelastic event for an incident electron is called the *Inelastic Scattering Cross-Section*. It is shown that the angular probability distribution for the plasmon range energy loss is a function of energy loss, primary beam energy and the scattering solid angle. The relationship is shown in Eq. 4.3 [37, 14].

$$\frac{d\sigma_{inelastic}}{d\Omega} \propto \frac{1}{\theta^2 + \theta_E^2} \quad Eq. 4.3$$

The left hand side of Eq.4.3 is the cross section of inelastic scattering for a small solid angle $d\Omega$. θ is the angle of scattering and θ_E the characteristic scattering angle (the full

width at half maximum of the angular distribution at an energy loss E) is $\Delta E/E$ or the ratio of the energy loss to the primary beam energy. This probability distribution is of a Lorentzian form. This effect of inelastic scattering in the diffraction pattern is the appearance of a background to the diffraction spots and broadening of the elastic features as the thickness of the sample increases. The mathematical description of this effect is expressed by the convolution of inelastic events cross-section with the intensity of the elastically scattered electrons as shown in Eq.4.4 [38].

$$\frac{dI_{inelastic}}{d\Omega} \propto \frac{dI_{elastic}}{d\Omega} \otimes \frac{d\sigma_{inelastic}}{d\Omega} \quad Eq. 4.4$$

Convolution of the elastic distribution with a Lorentzian function results in broadening of the intensity peak. This is seen in the diffraction pattern as a broadening by low angle inelastic scattering creating a halo around the diffraction spots. In fact, the angular distribution of inelastically scattered electrons is correlated with elastically scattered ones as shown by Eq. 4.3. It has been shown that, even by only letting the inelastic electrons existing in the vicinity of each diffraction maxima to contribute to the TEM image, images similar to an image fully constituted by elastic electrons can be produced [39]. This has been carried out by placing a small objective aperture near the diffraction peak which underlines the spatial correlation between the elastic and inelastic electrons [39]. In spite of this angular correlation, the contrast for Bragg reflections is highly reduced as these inelastic electrons are present in the vicinity of the elastic diffraction peaks. It has been shown in literature that by energy filtering the exit-wave

and only allowing the zero-loss electrons to enter the diffraction space, the contrast for Bragg reflections is drastically improved for crystalline samples [38]. Large angle inelastic scattering also create a background on a diffraction pattern, reducing the maximum contrast of the Bragg diffraction dots [39]. Thermal-diffuse scattering stemming from electron-phonon interactions are also present as a background in the diffraction pattern as an elastic signal with high momentum transfer [40]. Therefore, the phase contrast phenomenon is suppressed by the presence of the above-mentioned inelastic contributions in the diffraction patterns.

In fact, the possibility of decorrelating these elastic and inelastic scattering contributions in the diffraction plane more easily compared to doing so in the image plane, highlights the power of diffractive imaging. This would provide the basis for probing a specific elastic signal by filtering out the inelastic signals. By selecting a specific type of signal emanating from a specific interaction in the diffraction space (for example here by removing the inelastically scattered electrons), automatically, the effect of elastic interaction is manifested more intensely in the image in real space. In Ptychography, the aim is to retrieve the phase of the exit-wave by solving a set of equations in the diffraction space by assuming that the coherence of the beam is not completely lost. If this coherence is lost after the interaction with sample, the phase relation between the electrons in the diffraction pattern is lost and a correct phase retrieval is rendered impossible with the model developed beforehand. Unfortunately, this is the case for most commonly used samples in TEM that are prepared from the bulk of a material since extremely thin

samples cannot always be achieved easily by conventional sample preparation methods, as also noted before. To overcome this obstacle, it is proposed to enhance the coherence in the diffraction space via filtering out the inelastically scattered electrons. This will increase the contrast for elastic signal which is used by Ptychography to solve the phase equations. In the STEM setting, a magnetic prism is used to focus approaching electrons with a particular pattern (diffraction pattern) with the same energy to a point. Consequently, an energy-selecting slit is used to select a specific energy range to be used in the diffraction pattern and a set of lenses is used to reform the pattern with a narrow range of energies, ideally without any inelastic losses contributing to the pattern. The concern is that further propagation of the exit-wave in the spectrometer is affecting the phase. It could be argued that since the diffraction pattern is already in Fraunhofer plane (or the plane located at infinity), extra travelling, will not change the phase relation between the diffracted beams.

Chapter 5: Results and Discussion

In this chapter, the importance of Ptychographical phase reconstruction parameters are emphasized. Afterwards, ways to improve the reconstruction are explained. All the data shown in this chapter, except for those adapted and referenced, are acquired with an FEI Titan 80-300 KeV probe and image aberration corrected TEM/STEM. All the Ptychography experiments were conducted with an aberration corrected probe with either 80 or 200 KeV acceleration voltage specified in their section. The fast electron detector used is the Gatan K2 summit. The shutter speed for using the full field of CCD would be 400 frames-per-second (fps). The camera is located at the end of the Gatan Image Filter (GIF), which is essentially a magnetic prism for energy filtering the electron signal. This spectrometer can record images and diffraction patterns entering the spectrometer entrance aperture, filter electrons based on their energy using an energy-selecting slit after the magnetic prism, and reform the image or diffraction pattern with the remaining electrons.

The algorithm used for phase retrieval was the extended Ptychographical Iterative Engine (ePIE) which was explained in section 3.3. This algorithm was carried out by the MATLAB programming language. Several modules are used in this code. The generation module is creating the first guess of the complex valued probe function. The main ePIE module carries out the calculations described in 3.3. after it is fed with the system of coordinates and the 4D diffraction dataset. This module also calls another module responsible for subpixel shifting of the probe. The post processing module removes the

phase ramp in the phase reconstructed and crops the area of the object which has the highest overlap and plots it.

The filtering capability of the spectrometer will be used in the section 5.1 to improve the reconstruction quality. In section 5.2, resolving Phosphorus atoms in the lattice of Indium Phosphide (InP) and the experimental advantage of Ptychography over the HAADF signal is discussed. The effect of thickness is examined in section 5.3. Section 5.4 pertains to the experimentation of the novel technique called Moiré-Ptychography. The last section 5.5, is concerned with shedding light on the technical issues that the user of Ptychography technique should be aware of, whether they are acquiring or processing data.

5.1 Experimental Implementation of Energy Filtered CBED Ptychography

As mentioned in chapters 3 and 4, Ptychography works best when the sample under study is thin. Otherwise, the assumption of multiplicative behavior of the object function is not true. Propagation of waves inside the sample, inelastic scattering and dynamic diffraction are among the phenomena that are not considered by the current theory of Ptychography. In order to investigate the effect of energy filtering following the idea described in section 4.2, a Yttrium stabilized Zirconia (YSZ) sample was used. The YSZ sample used is estimated to be 50 nm thick, which is already thicker than what is usually used in Ptychography context. A 4D dataset of 86x85 diffraction patterns was acquired with the horizontal and vertical scanning step size of 0.2 Å. The rotation angle between scanning grid and the CBED was measured to be 88.95° for acceleration voltage of 200

KeV and a STEM camera length of 240 mm (in EFTEM mode). The dataset was binned by 8 times in u and v directions (i.e. horizontal and vertical directions of diffraction patterns) because this high data volume couldn't be processed within reasonable timespans. A Ptychographical phase reconstruction of the [010] zone axis is demonstrated in Figure 5.1.A&B. Figure 5.1.A shows that the heavier atomic columns (in red) are inducing a higher phase change compared to the blue regions which belong to the Oxygen sites. It is important to note that blue regions are showing also a positive phase change (around 0.74 radians) as suggested by the colour scale bar. In principle, if the thickness of the sample is thin enough that inelastic events can be neglected and the phase wrap phenomenon (see section 5.3) does not happen, what should be seen is that both heavy and light atomic columns appear as red circles on a blue background; heavier columns with a more intense red. In the practical setting of this experiment, this is not seen due to the fact that the atomic potential of the thick sample changes the phase of the incident electrons travelling between the atomic columns to an extent that is comparable to the electrons travelling in close vicinity of atomic columns. That is the reason a non-zero phase change is seen between Oxygen and Zr columns. The phase wrap phenomenon can also contribute to the loss of contrast of Oxygen columns in the background, as further will be described in section 5.3.

Spatially averaged diffraction pattern from a random area of the dataset acquired and a line scan showing the intensity plot taken from center of the bright field disk are shown in Figure 5.1.C&D. As can be seen, the multitude of Kikuchi lines and the

inelastically scattered electrons which are introducing visible broadening of the features in the bright field disk, are an indicator of the thickness of the sample. Since these intensities are interpreted by reconstruction software as frequencies in the Fourier space, the algorithm translates them into the image features by solving phase equations. This is equivalent of seeing all the electrons as elastic scattered electrons, which is incorrect.

In order to improve the reconstruction, energy filtering of the CBED patterns was performed following the discussion of section 4.2. Since the fast electron camera used is located at the after the energy-selecting slit of GIF, energy filtering of the diffraction patterns is possible. The diffraction pattern entering the spectrometer is then projected on the image plane of the prism and subsequently, the energy-selecting slits filters out the inelastic electrons. A 5 eV wide slit around the zero loss region (i.e. from -2.5eV to +2.5eV) was used to filter out the electrons with losses greater than 2.5eV . By doing so, the phase contrast from elastically scattered electron in the diffraction patterns would be highlighted. The red pixels (higher phase introduction) extended between the Zr columns in Figure 5.1.A are suppressed to a good extent in Figure 5.1.B as a result of energy filtering of the CBED.

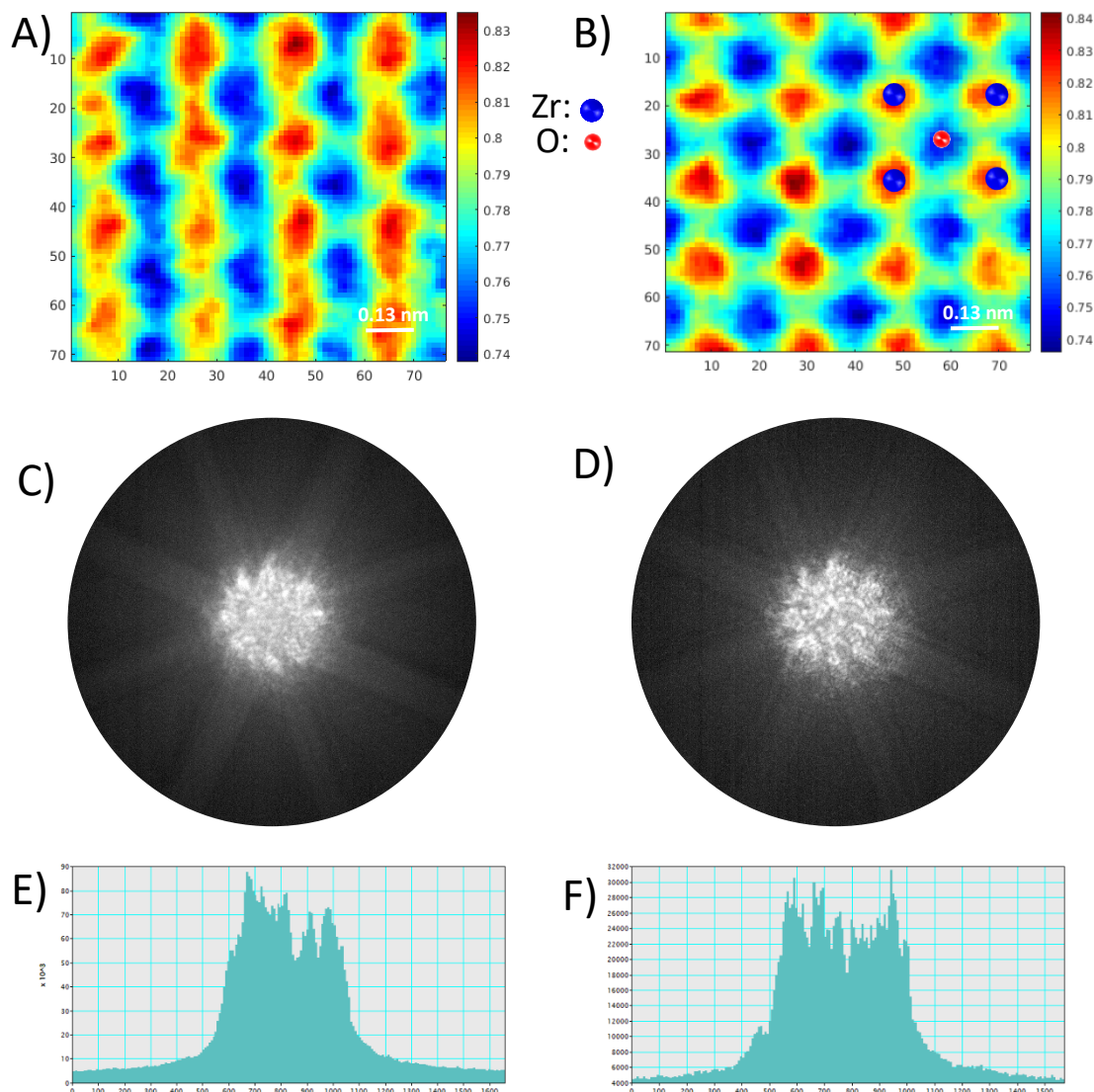


Figure 5.1 A) Phase reconstruction of the non-energy-filtered dataset ($dx=0.13 \text{ \AA}$); axes being the number of pixels B) Phase reconstruction of the energy-filtered dataset ($dx=0.13 \text{ \AA}$); axes being the number of pixels. The colour scale for A and B is shown on the right side of each. C) 25 Averaged diffraction patterns with unfiltered energy D) 25 Average diffraction patterns energy filtered E) Line profile of middle region of C F) Line profile of middle region of D showing higher contrast and finer details in Bright field disc compared to C

A straight band with green colour is seen in horizontal and vertical directions in the phase reconstruction of Figure 5.1.B, indicating that the phase in these regions has

changed more than the blue regions which is the location of Oxygen columns. This is attributed to the presence of Kikuchi lines in the diffraction patterns. The straight bands present in the diffraction patterns extending to higher frequencies without loss of intensity are translated by the ePIE algorithm as bands of intensity in the phase image reconstructed. In fact, one could confirm this by taking the back Fourier transform of an image consisted of lines of intensity in a dark background and plotting the phase of the Fourier transform as demonstrated in Appendix II. Therefore, higher phase indicated by the software between heavy atom (Zr) columns in horizontal and vertical directions of the phase reconstruction images is rather due to the presence of Kikuchi lines in the diffraction patterns than presence of atoms. In addition, the blue regions seen in between be higher intensity features and the disorder apparent between atomic columns seen in the phase reconstruction of both datasets, are an artefact of having a thick sample. Oxygen atoms are located in tetrahedral voids of the FCC crystal and hence, they should be seen in the phase reconstructed image ideally at the locations shown on Figure 5.1.B. The fact that the phase change caused by Oxygen atomic columns is not detected versus the background could be attributed to the extra scattering of electrons through the thickness of the matter, even after energy filtering. Light atoms are weak scatterers of electrons and hence, the peaks created by them in the diffraction patterns are expected to be of weak intensity. Due to sample thickness, thermal diffuse scattered (TDS) electrons and dynamical effects can screen the contrast of the features made by light atoms. Therefore, the thinner the sample is, the better the quality of the phase reconstruction

would be. Indeed, this would be very exclusive in terms of practicality of TEM analysis.

The thickness effects would be further investigated in section 5.2 and 5.3.

5.2 Resolving Light Atoms

As mentioned in chapter 3, the Ptychographical reconstruction has shown to be more sensitive to a weak electron scattering medium since it is utilizing phase as a contrast mechanism. In order to find out the optimum conditions for resolving the light atoms in a structure, a sample of Indium Phosphide was investigated. The sample is a FIB-prepared semiconductor device that was ion-milled after FIB lift-out for achieving a lower thickness than what can be provided by just FIB. The ion-milling process created a thickness gradient that ends in a hole in one of the FIB sample windows, as represented in Figure 5.2.A. Due to the thickness reaching zero at the edge of the sample, the thickness within the area where the Ptychography experiment was carried out had the t/λ of below 0.2 which is expected to be more suitable compared to a thick sample for the reconstruction. The calculated dose is $3.5 \times 10^7 \text{ e}^-/\text{\AA}^2$ and the screen current was below the detectable range of the measuring device (focusing screen) of the TEM (i.e. below 0.03 nA). since the camera used for recording the diffraction patterns is a direct electron detector, dose calculation is performed by summing up the signal above the dark noise and dividing it by scanned area. The convergence semi-angle of the probe was estimated to 19.5 mrad.

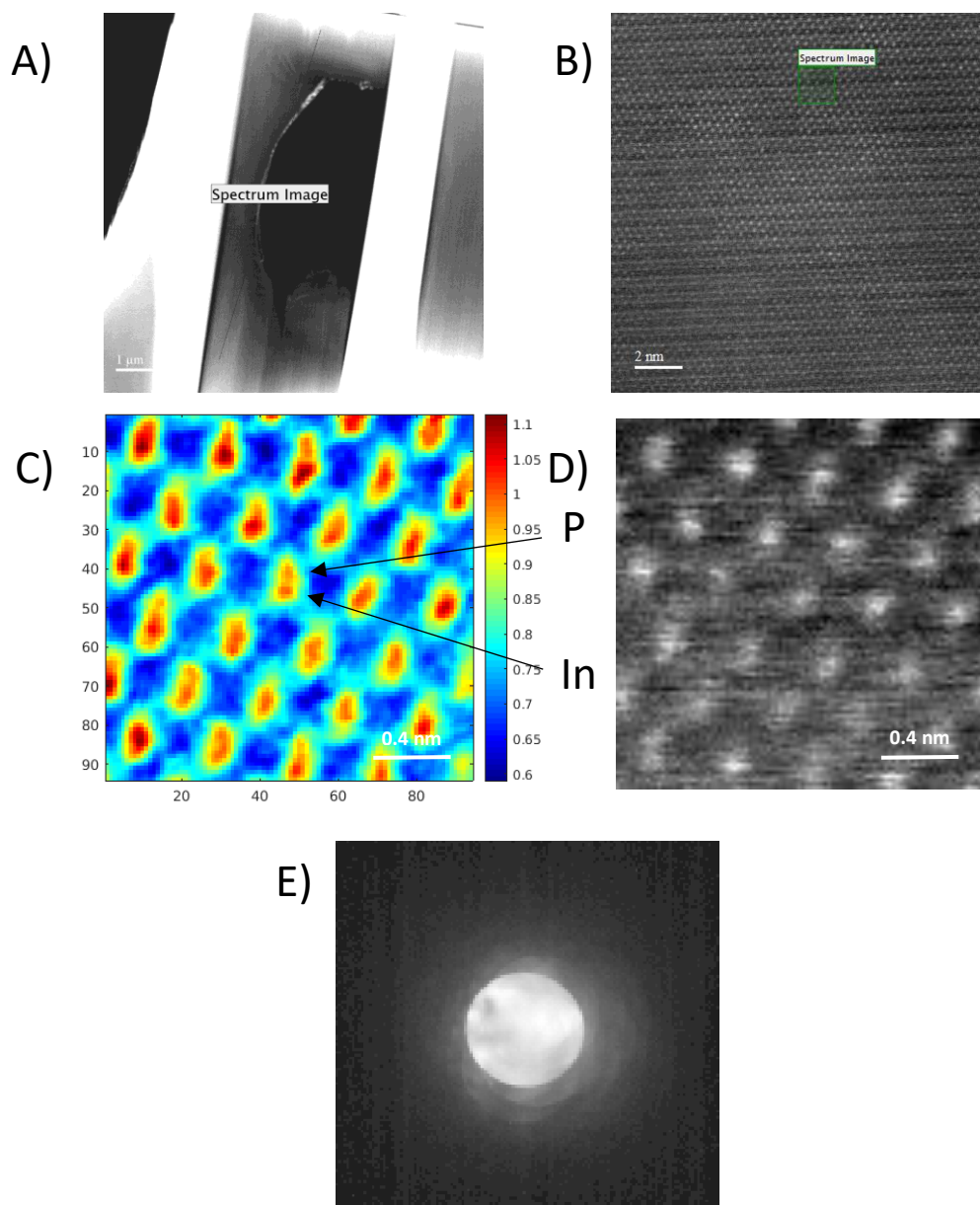


Figure 5.2 A) Low magnification image of the InP sample; B) Survey image showing the presence of CCD noise due to lower dose used; C) Ptychographical phase reconstruction from a thin area close to the hole, axes being the number of pixels ($dx=0.2 \text{ \AA}$) D) Synthetic HAADF signal reconstructed based on the set of diffraction patterns recorded on the CCD. E) 25 Averaged diffraction patterns from the 4D dataset. For comparison, look at Figure 5.1.C

The accelerating voltage used was 200 KeV and the STEM camera length was chosen to be 240 mm. The range of meaningful data in the diffraction pattern was

measured to extend to approximately 45 mrad (equal to 1.88 \AA^{-1}) and the higher frequencies of the diffraction patterns were not distinguishable from the dark noise of the K2 camera and hence, intensities at larger scattering angles were not included in the dataset to reduce the cost of calculations. The $(x,y,u,v) = (98 \times 98 \times 128 \times 128)$ dataset was generated by binning by 8 times in u and v directions from a 1024×1024 pixels to yield a 128×128 pixel diffraction patterns. The effect of data binning is described in section 5.6.

As depicted in Figure 5.2.C, the phase image reconstructed from the Ptychography algorithm is showing the presence of dumbbell shape atomic columns. Black arrows indicate the position of Indium and Phosphorous atoms. The synthetic HAADF signal made from the same dataset is shown in Figure 5.2.D. As a comparison, it is clearly visible that both In and P atoms are resolved in the Phase reconstruction whereas, in the HAADF signal generated from exactly the same dataset, the resolution is not favorable. Aside from the fact that the HAADF would not reveal the P atoms due to their low atomic number, the position of the In atoms are also determined with a considerable uncertainty due to presence of noise and beam induced Carbon contamination. The noise is partly stemming from the inaccuracies of the electronic unit rastering the probe on the sample. This would adversely affect the quality of the Ptychographical reconstruction as well since there would be a discrepancy between the system of coordinates defined for the ePIE algorithm by the number of scan points and their distances, and the actual positions where the probe has been placed. An algorithm for “Annealing” these inaccuracies of scanning has been proposed by Maiden et al [41]. This algorithm is based on calculating a number of

sub-pixel shifted Fourier transforms around each defined scanning point and select the one having minimum error compared to others for the next iterations. This approach is not directly measuring the amount of scanning inaccuracy but assumes, by minimizing the error metric defined in section 3.3, that the scanning error is accounted for. Although this assumption improves the reconstruction quality by virtually compensating for scanning imprecision in phase reconstruction process, the cost of calculations is highly increased due to calculation of several forward and backward Fourier transforms that are not used in the final reconstruction. The other source of the noise seen in the synthetic HAADF signal is the lower dose used for the Ptychography experiment compared to a normal HAADF STEM imaging condition imposed by a thin sample. The fact that a Ptychographical reconstruction could reveal the structure with less sensitivity, apart from showing the advantage of Ptychography in low dose conditions, is due to its use of all the information in diffraction space, not only a certain range of angles as used by ADF.

The fact that the HAADF signal underperforming the Ptychography reconstruction, could be attributed to two more factors. Firstly, since the HAADF image contrast comes from the elastic scattering power of atomic potential, the efficiency of this signal is low when the scattering factor (Z or atomic number) or the thickness of the scattering medium is low. The ratio of intensity of the HAADF signal to the intensity of the primary beam drops drastically as the thickness decreases below a certain level [42]. This would justify the lack of adequate contrast for this extremely thin part of the sample used, especially for the Phosphorous atomic columns. Secondly, although the STEM probe is

aberration corrected, the focus and astigmatism conditions may not be fully tailored for the HAADF; although it was corrected to the best possible extent. This experimentally confirms the lower sensitivity of Ptychography to defocus and other aberration conditions of the probe, due to the deconvolution of the probe. To summarize the differences between the HAADF synthetic signal and phase reconstruction, the effect of scanning noise on both reconstructions were explained. Moreover, advantages of the Ptychographical phase reconstruction over the HAADF signal in the face of low dose and low specimen thickness were highlighted. In addition, taking advantage of the entire information contained in the diffraction pattern by phase reconstruction exhibited the power of Ptychography in resolving more structural information; especially the light atomic columns.

5.3 The effect of specimen thickness

The presence of a thickness gradient ending in a hole in the InP sample, provided a good opportunity for inspecting the effect of thickness on phase reconstruction. The phase reconstruction of a thicker part of the sample (t/λ of around 0.4) and the synthetic HAADF signal is depicted in Figure 5.3 A&B. The acquisition parameters were deliberately chosen to be identical to the one presented in section 5.2 for having a firm ground for comparison, except for the number of diffraction patterns acquired (86x84x128x128). In contrast to Figure 5.2.C, the presence of dumbbells is less conspicuous. This could be seen as arising from higher number of diffusely scattered electrons in the diffraction patterns

due to increased thickness of the sample. The InP dumbbells also seem to be more delocalized in this thick part of the sample reconstructed than what is seen in Figure 5.2.C due to higher beam propagation distance through the sample causing dynamical effects and propagation of the electron beam from one column to a neighbouring column.

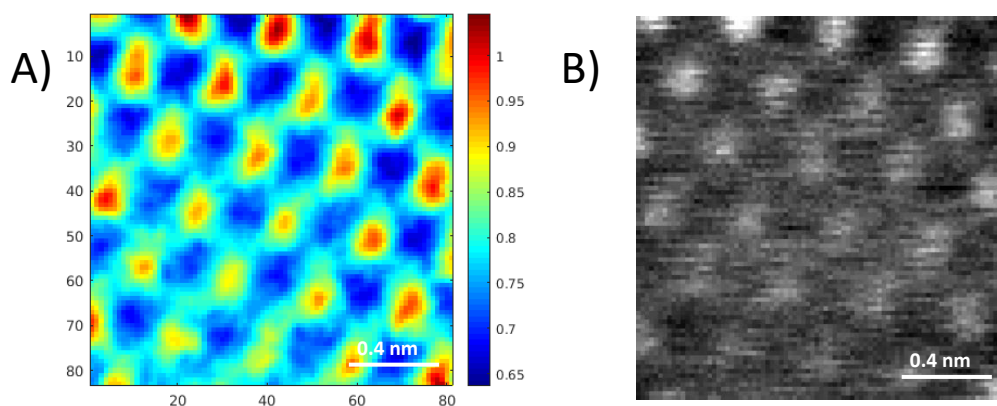


Figure 5.3 A) Ptychographical phase reconstruction from a thicker area farther from the hole, axes being the number of pixels ($dx=0.2 \text{ \AA}$) B) Synthetic HAADF signal

Another factor making the contrast interpretation challenging for the retrieved phase when the sample is thick, is the *Phase Wrap*. If the phase of the incident electron wave is changed more than 2π , for example $2\pi + \varphi$, the phase change is equivalent to φ . Hence, *Contrast Reversal* can happen as the thickness of the crystal overshoots a certain value. This means the heavier atomic columns may have a lower phase value than the lighter columns and appear darker in the reconstructed phase image, as shown in Figure 5.4 adapted from [28]. As shown in the multi-slice simulation results of this figure, as the thickness of the specimen reaches 20 unit cells and above, the phase reconstructed of Gallium atomic columns in a GaN sample resets to zero after 2π phase change.

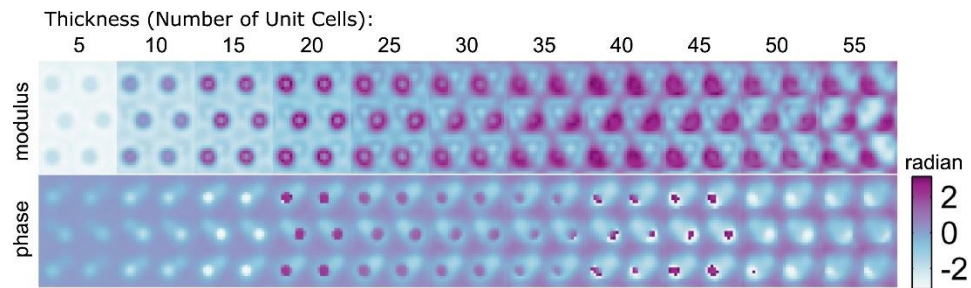


Figure 5.4. Computer simulations of object transfer function retrieval via Ptychography for different thicknesses of GaN. Contrast reversal happens at around 20 unit cells and Ga atoms appear darker than N atoms in phase [28].

For this reason, Gallium atoms are appearing darker compared to Nitrogen atoms in the reconstructed phase image when the material is more than 20 unit cells thick. Higher thickness also coincides with higher probability of dynamic diffraction, inelastic scattering and other beam propagation effects which are not fully taken into account in the mathematical multiplicative model proposed by Ptychography algorithm. Therefore, in higher thicknesses, the GaN dumbbells seem more delocalized compared to when phase retrieval of fewer unit cells is intended. By a similar analogy, the contrast loss for Indium columns in Figure 5.3.A compared to 5.2.C could be attributed to the phase wrap and beam propagation effects through the sample. Therefore, neglecting the higher beam damage for the thinner samples, as Williams and Carter state in their textbook [7], the TEM motto “*thinner is better*” still holds true!

5.4 Experimental Implementation of Moiré-Ptychography

The experimental fulfillment of the Moiré-Ptychography is presented in Figure 5.6. The experiment was conducted on a YSZ substrate in [010] zone axis with 200 KeV electrons. A dataset of 90x90 diffraction patterns, each 256x256 pixels (after binning) was acquired. The desired step size (d_s) was chosen to be 0.21 Å and the lattice parameter was known from literature to be 5.158 Å [43]. Therefore, d_c being half of the lattice parameter, the total scanning step size was 2.79 Å. Although the thickness of the specimen is not ideal for Ptychography, the experiment is serving as a proof of concept. The green square in the survey image shown in 5.6.A contains 90 scanning points in each direction from 48^2 unit cells (or 96^2 2D unit cells) to recover $\sim 2^2$ unit cells. The result of phase reconstruction is shown in Figure 5.6.C. Figure 5.6.B shows the convergence of the ePIE algorithm after 200 iterations by error metric described in section 3.4.2.

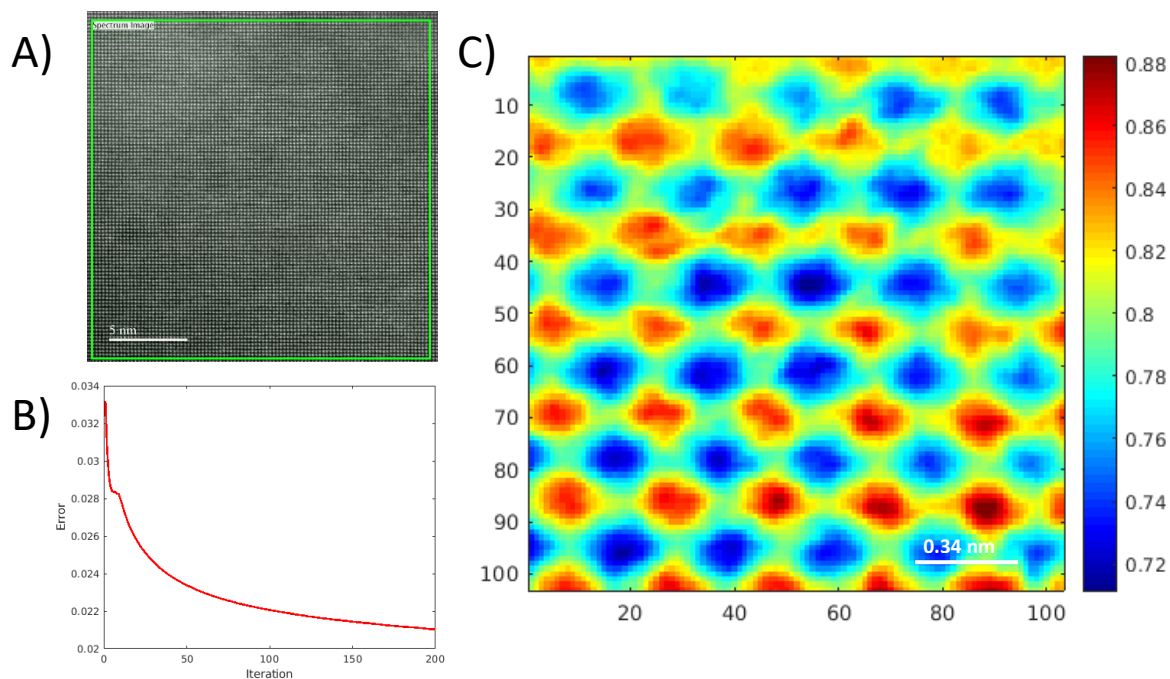


Figure 5.6 A) Survey image, the green square showing the range of data collection B) Error curve for ePIE algorithm showing the convergence of the algorithm C) Phase reconstructed for 4 unit cells, axes being the number of pixels ($dx=0.17 \text{ \AA}$)

5.5 Ptychographical Reconstruction Troubleshooting

In most cases, the Ptychographical reconstruction doesn't generate the desired results due to either miscalibration of the parameters on the microscope or entering wrong parameters in the reconstruction software. This section addresses the effects of some of the most important Ptychographical reconstruction parameters and concerns the practicalities of implementation.

- **Beam Damage**

Since the sample used for Ptychography should be infinitesimally thin, the effect of beam damage is important. Another reason that paying attention to the dose used is that the scanning dwell time currently used by even the fast electron detectors, are longer than the STEM HAADF because the whole field of view of the diffraction pattern must be recorded. On the other hand, if the electron dose or the beam current is not high enough, the diffraction patterns would not have a good signal to noise ratio and the contrast in phase reconstruction would not be meaningful. Thus, there is a certain optimal range in which the reconstruction yields a trustable result. Although the dose effect study is not completely performed in the current work, the Ptychography experiments presented in this section introduce a finding which suggests a rough estimate of the maximum dose for thin materials is presented.

Figure 5.7 is showing 2 survey images after two separate Ptychography 4D dataset acquisition of the same InP sample discussed in section 5.2 with different electron dose or beam current. Figure 5.7.A is conspicuously showing the effect of beam damage causing mass loss after the dataset is acquired. The electron dose used is $2.3 \times 10^9 \text{ e}^-/\text{\AA}^2$ and the phosphorous screen read-out was 150 pico-amperes while acquiring the data. It is worthy to note that this beam current is the conventional value used for STEM HAADF imaging. This underlines the low dose nature of this technique and shows that, on thinner samples, the dose used must be much lower than what is

commonly used in HAADF atomic resolution imaging if we aim a high-quality signal. Figure 5.7.B shows the phase reconstructed from the area surrounded by the green dashed circle in figure 5.7A and C. The scanning is performed in rows from left to right and from top to bottom. It is evident, from the phase reconstruction, that in the initial moments of data acquisition, the signal is strong and the contrast is of high value in the upper parts of the image. As the beam is rastering forward, the beam damage is introduced to the sample such that the lower parts of the reconstruction barely have any meaningful signal due to mass loss. The solution for these cases is either using a lower dose or using a higher camera shutter speed. The diffraction patterns used for this reconstruction are originally 1920x1870 pixels but as will be proven in the next bullet point of this section, such a detailed diffraction pattern is not adding to the resolution indeed. Thus, since using less CCD pixels allows a higher shutter speed, using a smaller diffraction pattern would lead to a gain from a dose rate perspective. Figure 5.7.C shows the survey image after data acquisition for the reconstruction shown in section 5.2. The mapped area is marked with a green dashed circle. As manifested, the beam damage is significantly less severe with the dose $3.5 \times 10^7 \text{ e}^-/\text{\AA}^2$ used. A set of experiments is needed in order to reach for detection of the minimum dose generating good quality reconstructions. It is at least evident here that the maximum dose used shall not exceed $\sim 10^7 \text{ e}^-/\text{\AA}^2$ for InP and similar samples. It is not necessary (or may even be detrimental in thin samples) to use the settings normally used on STEM imaging when doing a Ptychography experiment.

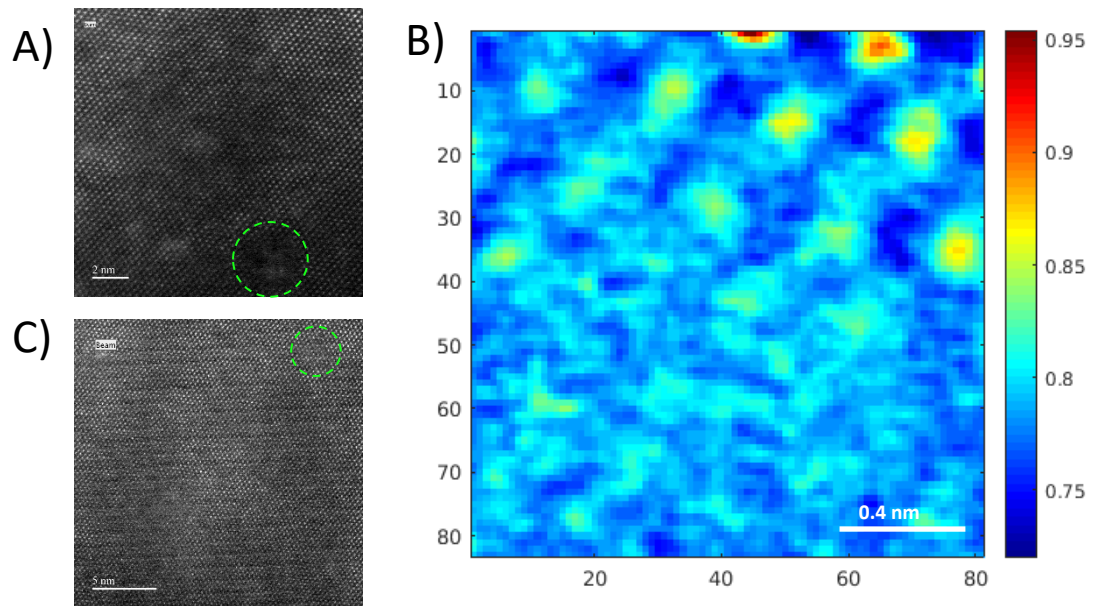


Figure 5.7. A) survey image after Ptychography dataset acquisition with electron dose of $2.3 \times 10^9 \text{ e}^-/\text{\AA}^2$ or 150 pA screen current. The approximate mapped area is shown by a green dashed circle. B) Phase reconstruction of the dataset acquired from A. C) survey image after Ptychography dataset acquisition with $3.5 \times 10^7 \text{ e}^-/\text{\AA}^2$ with the screen current being below the detectable range for the phosphorous screen of the TEM used (30 pA). the phase reconstruction for C is shown in Figure 4.2.C.

- **Data Binning**

Ptychography datasets occupy a great deal of storage space. The 4D datasets acquired in the current work were acquired on 1920x1870 pixel CCD (after binning by two times in each direction) in a 16-bit format. The usual dataset contains at least 80x80 diffraction patterns and the dataset size is more than a couple tens of Gigabytes. Performing an iterative algorithm for more than a hundred iterations on such a big dataset will require an unreasonable amount of time of processing. Some solutions are proposed for overcoming this problem. The first and foremost solutions would be increasing the processor power either by improving CPU power or adapting the ePIE algorithm to

parallel processing which is a challenging task. The reason is that ePIE uses the previous guesses of the object and probe functions in the next iteration. For parallel processing this algorithm, it would be necessary to divide the object (and the 4D dataset) into subsets to assign the reconstruction of each subset to a different CPU. Although this seems promising, this approach introduces artifacts in the borders of reconstruction since the borders have not used all the redundant information present in adjacent subsets. Algorithms for overcoming this issue have been proposed in the literature [44] which are based on estimating the phase of the object transfer function in the borders of subdivided regions and “stitching” the subsets together.

The other approach is to reduce the data size via binning and using the dataset for reconstruction as a whole. The datasets were binned for the current work with bi-cubic interpolation in the diffraction space. The effect of data binning on phase reconstruction is demonstrated in Figure 5.8. Reconstruction of a 4D dataset acquired from a unit cell of a YSZ crystal with identical reconstruction parameters except for binning has been performed. Figure 5.8 A, B and C are the phase reconstructed images of the 4-, 8- and 16-times binned datasets respectively. The 4- and 8- times binned reconstructions do not show a noticeable change, which means that the reconstruction can be done 16 times faster compared to the original dataset without severe loss of quality. Binning data more than 8 times seems to have an adverse effect on the quality of reconstruction as shown in Figure 5.8.C. It can be concluded that in 16 times binned data, there are not enough pixels to describe the fine details of the diffraction patterns. Another practical method of

reducing the data size is to cut-out the range of the pixels in the diffraction that contain meaningful signal in the high frequency. For the most cases performed in this thesis, only approximately half of the pixels in horizontal and vertical directions of the CCD directions contain meaningful signal and the information in the higher frequency range is lost in the K2 camera dark noise (15 electron counts per pixel in a 2 times binned dark reference image).

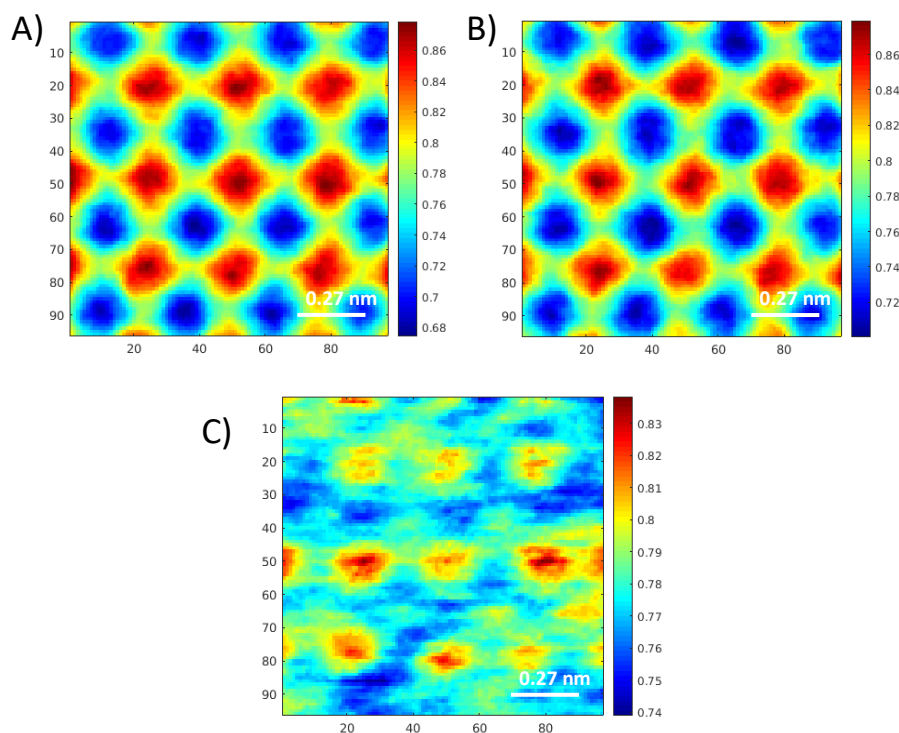


Figure 5.8. Effect of data binning. Original data binned by A) 4 B) 8 and C) 16 times in u and v directions in the diffraction space

- **Wrong or miscalibrated reconstruction parameters**

The reconstruction process can be regarded as an interference pattern itself.

Complex value of each of the subsets of the object in real space is determined by the

backward Fourier transform of the subset when the amplitude of it has been substituted by the diffraction pattern collected from that region. The Fourier transform of each subset can be regarded as a recipe of spatial waves with different frequencies and directions in real space. The addition of all the wave patterns of all the subsets of the object in real space, constitutes the object transfer function. In the context of atomic resolution Ptychography, visualization of higher phase regions (atomic columns) can be achieved only when these spatial waves interfere in a constructive manner. The empty space between atoms accordingly, can be interpreted as if the spatial waves have interfered in a destructive manner. With this analogy in mind, the definition of the scanning point in the coordinate system is extremely important. For example, in a case that one of the scanning points corresponding to an atomic column is intentionally defined on the space between two other atomic columns, this would cause the contrast between the two atomic columns to be suppressed. The spatial information is precisely encoded in the diffraction pattern and therefore, it is crucial for the reconstruction that the real space scanning coordinates defined are corresponding correctly to this information. Any mismatch between the reconstruction parameters and experimental conditions results in loss of contrast and accuracy of the reconstruction.

The most effective reconstruction parameters are: scanning step size, rotation angle between CBED patterns and the scanning grid and the pixel size in diffraction space (dk). The effect of miscalibration of these parameters on the contrast of the

final reconstruction is summarized in Figure 5.9. For measuring the sensitivity of the reconstruction on the spatial coordinates, the same dataset from a unit cell of YSZ used in the “Data Binning” section was used. A set of reconstructions with 15 iterations were made with varying step size and rotation angle in the software to detect the artifacts of having parameters different from the experimental settings. The variance of the pixels in the reconstructed region of the object was used as a measure of the reconstruction quality by changing scanning step size and rotation angle in Figure 5.9.A and B. It is evident that the correct values of the scanning step size (0.19\AA) and rotation angle (72°), which are known since they are selected by the user at the time of experiment, maximize the variance of the pixels in the phase of object reconstructed. Two miscalibrated cases are shown in Figure 5.9.C and D. Figure 5.9.C shows a phase reconstruction of the object with step size of 0.415\AA , almost twice the actual step size. The pixelated reconstruction is an artifact of having a step size greater than the experimental value. The reason for pixilation is that the pixel size is predetermined by the value of dk and when a greater step size is defined, more pixels are needed than what is necessary for describing the object. In other words, the intensity is not continuous due to the presence of dark and bright pixels side by side. In the diffraction pattern, since the number of pixels and the length ($1/\text{\AA}$) of each pixel is fixed, the extent of information encoded in it is fixed. When the back Fourier transform is made to translate reciprocal space to real space information, a bright spot exists in the middle of the subset due to the shape of the CBED (having a bright

circle at the center). That is the reason a bright spot is seen in the object at the location of every scanning point and the spacing between them is darker since the intensity in the diffraction pattern encoded for these pixels is faint or missing. As an analogy, one can think of having the continuous pattern of intensity and padding every one pixel with a dark pixel to get Figure 5.9.C. With this analogy, the separated bright pixels are creating a pattern on a dark background whereas in a correct reconstruction, the bright regions representing atomic columns must be continuous and have no dark pixels inside. Figure 5.9 D shows a phase reconstruction with a wrong rotation angle 117° instead of the original 72° . As seen in the figure, the reconstructed phase image shows a higher contrast in the peripheries of the reconstructed region. The reason is that, in these areas, less subsets are interfering and therefore, the contrast is not degraded as heavily as in the middle where the percentage of redundancy is higher. Therefore, if the rotation angle is not calibrated, the contrast in the reconstruction region is degraded most in the main reconstruction region. In most cases, when the reconstruction parameters were chosen incorrectly, the algorithm still converges. This would be more subtle and problematic since it is not conspicuous that the results are invalid compared to when the algorithm diverges. Hence, it can be concluded that calibration of the measurement parameters before doing the experiment is of vital importance.

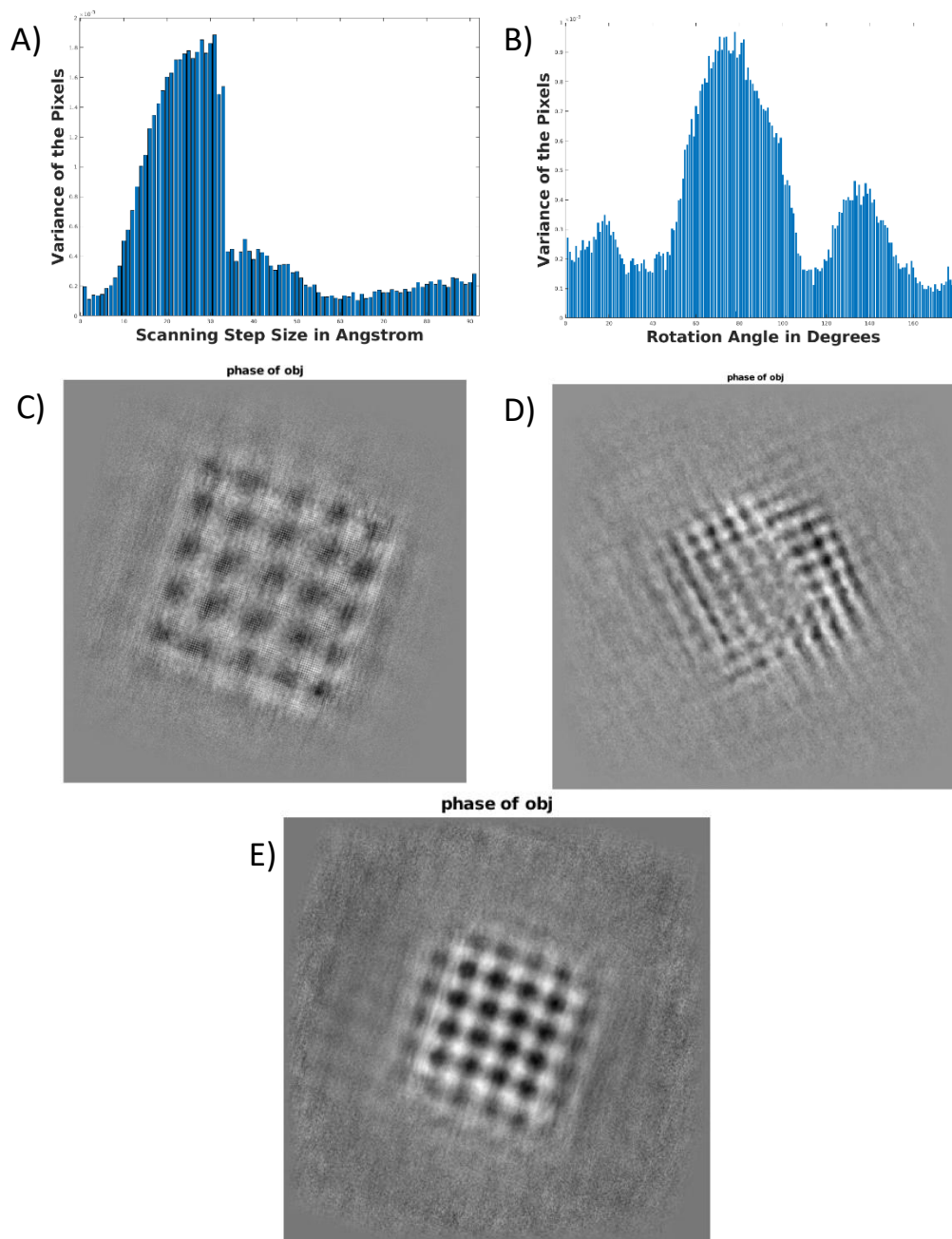


Figure 5.9. A) Variance of the pixels in the object phase reconstructed plotted versus the scanning step size varying from 0.05 to 0.5 Å. Maximum contrast appears when the scanning step size is entered the software correctly. B) Variance of the pixels in the object phase reconstructed plotted versus the rotation angle between CBED and scanning grid. Object phase reconstructed with: C) step size larger than correct value; D) rotation angle different from correct value and E) with correct scanning step size and rotation angle

- **Beam convergence angle**

The convergence angle of the beam is determining the degree of overlap between the diffracted spots. As explained in chapter 3, a larger convergence angle allows more overlap between the diffracted disks and thus, more measurable intensities, ultimately increasing the number of known versus unknown variables in the equation sets. The effect of convergence angle was also investigated by choosing a lower convergence angle compared to the experimental setting discussed in section 5.2. For the experiment resulted in phase reconstruction shown in Figure 5.10.A, a $30\mu\text{m}$ C2 aperture was chosen corresponding to convergence angle of 11.3 mrad.

In the case of Figure 5.10, since the percentage of disk overlap, and hence the number of measured intensities, is less than the number of unknown phase components in phase equations due to lower convergence angle (see section 3.2), divergence of the ePIE algorithm happens. An image of the reconstruction and the error plot are shown in Figure 5.10.B&C. It is important to mention that the sample and the experimental parameters are identical to the case presented in section 5.2. except that the beam convergence angle used in the reconstruction is smaller.

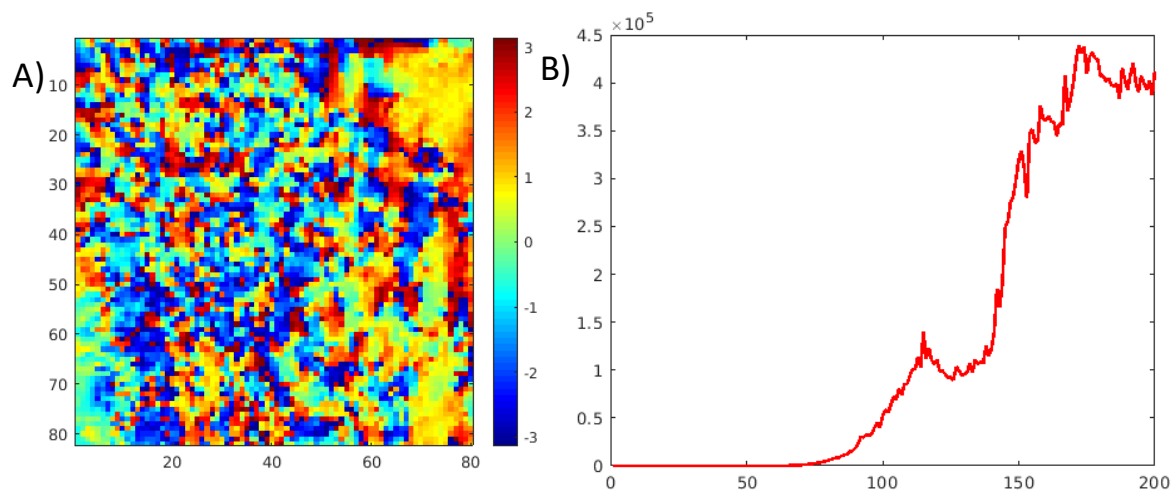


Figure 5.10.A) Diverged phase reconstruction B) Error metric plot showing the divergence of the algorithm due to lower convergence of the beam

A useful study of other practical issues of phase reconstruction process via simulations has been carried out by Latychevskaja [45] which is strongly suggested to the reader interested in furthering knowledge on additional potential problems of Ptychography.

Chapter 6: Conclusions and Prospects

Throughout this thesis, attempts were made to explain the concepts of resolution as well as the importance of improving resolution and barriers in achieving higher resolution. The working principles of Transmission Electron Microscopy and basic information needed for further discussions were covered. The phase problem was expressed and means of recovering it were covered in the literature review. Electron Ptychography was demonstrated to be a powerful technique of phase retrieval in spite of the practical difficulties. Iterative and analytical solutions in Ptychography were described and pros and cons of them were reflected upon. A comparison of electron Ptychography with other well-established methods in STEM, in the context of having higher resolution (especially for light atoms) was made. As a contribution to the field of Electron Ptychography, two novel methods of sampling in data acquisition and data collection, namely Moiré-Ptychography and CBED Energy Filtering, were introduced. The advantages of the latter and the former as approaches to reduce dose and increase signal coherence were underlined. The experimental execution of the two new methods was conducted successfully. Results from validation experiments were presented and the limitations of this technique were illustrated. Caveats of phase reconstruction were outlined and the sensitivity of the algorithm regarding different parameters such as specimen thickness, convergence angle of the probe and the effect of the miscalibration of the initial parameters was reviewed.

The current Ptychographical reconstruction approach imposes great constraints on the sample. The sample thickness requirements are very stringent for a viable

reconstruction and is significantly smaller than the practical thickness achievable by current TEM sample preparation techniques in a controllable way. Preparing a sample with Focused Ion Beam (FIB) sample preparation technique around 25-30nm thick, which is still considered large in Ptychography context, takes a long time and needs intricate equipment according to the FIB literature [46]. Therefore, it can be concluded that the existing theory of Ptychography is not easy-to-use and fully applicable to the majority of the existing samples as is. This obstacle shall be removed either by developing a more inclusive Ptychography theory or precisely thin and clean sample preparation methods. The former seems to be more promising than the latter in TEM field of research.

Although the idea of Moiré-Ptychography was explained and the experimental implementation of this novel technique was demonstrated on a cubic crystal, a further exploration of the technique is needed. Although the general theory of this technique proves the possibility of execution on more complicated samples, achieving promising experimental results remains a challenging task. The theory is assuming that the 2D unit cell is recurring in a large field with no variation in structure. In contrast, if a non-uniform strain field exists in the material, the transformation matrix is not sufficient for bringing the crystal space to the orthonormal space. In fact, since the Moiré sampling is more sensitive to the presence of strain fields in the material, compared to conventional oversampling used in STEM imaging, developing a more adaptive sampling theory seems crucial.

Another idea to be followed for having a better definition of the space coordinates and scanning noise treatment is using the diffraction pattern itself. It has been shown that the features in the bright field disk (as well as dark field disks) are changing as a function of the relative positioning of the probe on the unit cell. Indeed, these features are very sensitive to change in position. Thus, regardless of the extent of scanning inaccuracy, the exact position of the probe is already encoded in the diffraction pattern by the features of the bright field disk. It is possible to directly extract the real space location information if a thorough theory explaining the dependency of bright field disk features on the atomic environment that the probe "sees" exists. With such a theory, scanning noise is not detrimental to the phase reconstruction since the scanning grid matrix is calculated directly from interpretation of the features within diffraction patterns and there is no need to force the reconstruction software to stick to the rectilinear mesh defined. The counter argument for this idea is that, for predicting such correlation between the bright field disk features and position of the probe, preliminary information about the sample structure is needed. It could be true that sometimes, a totally unknown material is being characterized but, in most cases, preliminary information exists, at least from STEM HAADF signal.

Appendix I

2D Fourier Transform:

$$\mathcal{F}\{f(x, y)\} = \iint f(x, y)e^{2\pi i(ux+vy)} dx dy = F(u, v)$$

2D Inverse Fourier Transform:

$$\mathcal{F}^{-1}\{F(u, v)\} = \iint F(u, v)e^{-2\pi i(ux+vy)} du dv = f(x, y)$$

Convolution Integral:

$$f(x, y) \otimes g(x, y) = \int f(u, v)g(x - u, y - v) du dv$$

Fourier Convolution Theorem:

$$\mathcal{F}\{f(x, y) \cdot g(x, y)\} = \mathcal{F}\{f(x, y)\} \otimes \mathcal{F}\{g(x, y)\} = F(u, v) * G(u, v)$$

Dirac Delta Function:

$$\delta(u - u_0, v - v_0) = \begin{cases} 0 & \text{for } u \neq u_0 \text{ and } v \neq v_0 \\ \infty & \text{for } u = u_0 \text{ and } v = v_0 \end{cases}$$

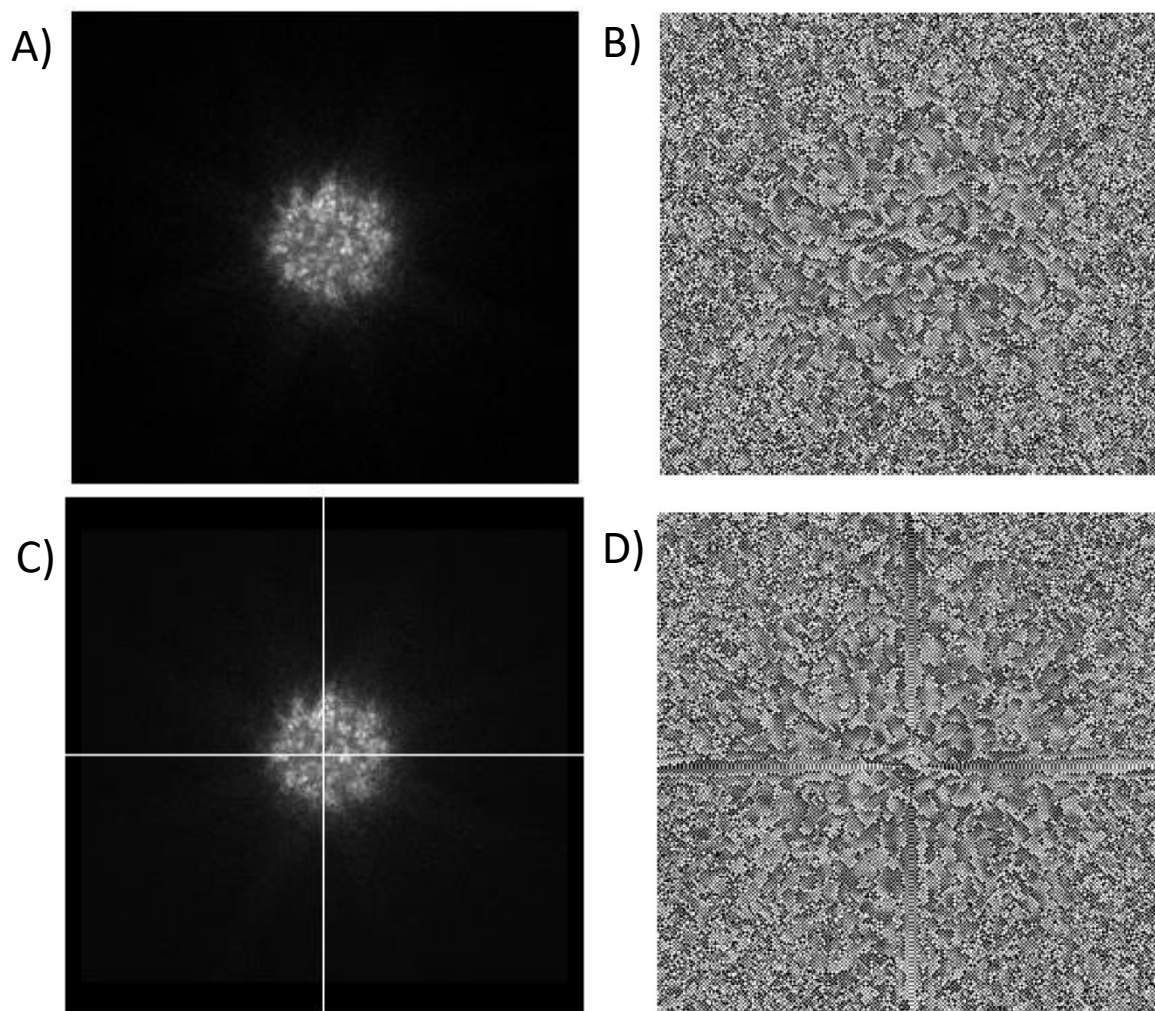
$$\text{such that: } \int \delta(u - u_0, v - v_0) du dv = 1$$

Convolution with a Delta Function or “Sifting Property”:

$$F(u, v) * \delta(u - u_0, v - v_0) = F(u_0, v_0)$$

Appendix II

The effect of presence of straight lines in the CBED is shown in Appendix Figure 1. 1.A shows a randomly selected diffraction pattern collected from a YSZ sample. 1.B shows the phase of the back Fourier transform of this pattern. In order to investigate the effect of Kikuchi bands, high intensity horizontal and vertical lines were added to this CBED as shown in 1.1.C. The back Fourier transform of the new CBED shows that horizontal and vertical bands of contrast appear in the phase of this Fourier transform which are not seen in the original Fourier transform of the CBED. This would justify the higher phase values between the Zr atomic columns in horizontal and vertical directions as compared to diagonal directions in Figure 5.1.A&B.



Appendix Figure1. A) a CBED collected from a YSZ sample described in section 5.1. B) Phase of the backward fast Fourier transform of A. C) Horizontal and vertical lines added to A to serve as Kikuchi lines. D) Backward fast Fourier transform of C showing an intensity change applied by virtual Kikuchi lines

References

- [1] Under the microscope by William J. Croft, ed., vol. , , : Books.google.be, 2006, p. .
- [2] [Online]. Available:
https://commons.wikimedia.org/wiki/File:Chromatic_aberration_lens_diagram.svg.
- [3] [Online]. Available: <https://upload.wikimedia.org/wikipedia/commons/6/6e/Lens-sphericalaberration.png>.
- [4] S. G. Lipson, H. Lipson and D. S. Tannhauser, "Optical Physics: History of ideas," , 1995.
- [5] P. J. Goodhew, Electron microscopy and analysis, 1988.
- [6] F. Haguenau, P. Hawkes, J. Hutchison, B. Satiat–Jeunemaître, G. Simon and D. Williams, "Key events in the history of electron microscopy.," *Microscopy and Microanalysis*, vol. 9, no. 2, pp. 96-138, 2003.
- [7] C. B. Carter and D. B. Williams, Transmission Electron Microscopy: A Textbook for Materials Science, 1996.
- [8] R. Erni, Aberration-Corrected Imaging in Transmission Electron Microscopy: An Introduction, 2015.
- [9] S. Findlay, N. Shibata, H. Sawada, E. Okunishi, Y. Kondo and Y. Ikuhara, "Dynamics of annular bright field imaging in scanning transmission electron microscopy," *Ultramicroscopy*, vol. 110, no. 7, pp. 903-923, 2010.
- [10] A. Tarantola, Inverse Problem Theory and Methods for Model Parameter Estimation, 2004.
- [11] R. P. Millane, "Phase retrieval in crystallography and optics," *Journal of The Optical Society of America A-optics Image Science and Vision*, vol. 7, no. 3, pp. 394-411, 1990.
- [12] J. Miao, R. L. Sandberg and C. Song, "Coherent X-Ray Diffraction Imaging," *IEEE Journal of Selected Topics in Quantum Electronics*, vol. 18, no. 1, pp. 399-410, 2012.
- [13] J. M. Rodenburg, "Ptychography and Related Diffractive Imaging Methods," *Advances in Imaging and Electron Physics*, vol. 150, no. , pp. 87-184, 2008.
- [14] S. J. Pennycook and P. D. Nellist, "Scanning transmission electron microscopy : imaging and analysis," , 2011.
- [15] G. Chartier, "Introduction to optics," , 2005.

- [16] R. W. Gerchberg, "A practical algorithm for the determination of phase from image and diffraction plane pictures," *Optik*, vol. 35, no. 2, pp. 237-246, 1972.
- [17] J. Barthel, "Dr. Probe: A software for high-resolution STEM image simulation," *Ultramicroscopy*, vol. 193, pp. 1-11, 2018.
- [18] A. M. Maiden, M. J. Humphry, F. Zhang and J. M. Rodenburg, "Superresolution imaging via ptychography," *Journal of The Optical Society of America A-optics Image Science and Vision*, vol. 28, no. 4, pp. 604-612, 2011.
- [19] J. M. Rodenburg and H. M. L. Faulkner, "A phase retrieval algorithm for shifting illumination," *Applied Physics Letters*, vol. 85, no. 20, pp. 4795-4797, 2004.
- [20] A. M. Maiden and J. M. Rodenburg, "An improved ptychographical phase retrieval algorithm for diffractive imaging," *Ultramicroscopy*, vol. 109, no. 10, pp. 1256-1262, 2009.
- [21] Y. Jiang, Z. Chen, Y. Han, P. Deb, H. Gao, S. Xie, P. Purohit, M. W. Tate, J. Park, S. M. Gruner, V. Elser and D. A. Muller, "Electron ptychography of 2D materials to deep sub-ångström resolution," *Nature*, vol. 559, no. 7714, pp. 343-349, 2018.
- [22] J. M. Rodenburg and R. H. T. Bates, "The theory of super-resolution electron microscopy via Wigner-distribution deconvolution," *Philosophical Transactions of the Royal Society A*, vol. 339, no. 1655, pp. 521-553, 1992.
- [23] P. Li, T. B. Edo and J. M. Rodenburg, "Ptychographic inversion via Wigner distribution deconvolution: Noise suppression and probe design," *Ultramicroscopy*, vol. 147, no. 147, pp. 106-113, 2014.
- [24] H. Yang, R. N. Rutte, L. Jones, M. Simson, R. Sagawa, H. Ryll, M. Huth, T. J. Pennycook, M. Green, H. Soltau, Y. Kondo, B. G. Davis and P. D. Nellist, "Simultaneous atomic-resolution electron ptychography and Z-contrast imaging of light and heavy elements in complex nanostructures," *Nature Communications*, vol. 7, no. 1, p. 12532, 2016.
- [25] O. Bunk, M. Dierolf, S. Kynde, I. Johnson, O. Marti and F. Pfeiffer, "Influence of the overlap parameter on the convergence of the ptychographical iterative engine.," *Ultramicroscopy*, vol. 108, no. 5, pp. 481-487, 2008.
- [26] R. R. Meyer and A. I. Kirkland, "Characterisation of the signal and noise transfer of CCD cameras for electron detection.," *Microscopy Research and Technique*, vol. 49, no. 3, pp. 269-280, 2000.
- [27] H. Yang, L. Jones, H. Ryll, M. Simson, H. Soltau, Y. Kondo, R. Sagawa, H. Banba, I. MacLaren and P. D. Nellist, "4D STEM: High efficiency phase contrast imaging using a fast pixelated detector," *Journal of Physics: Conference Series*, vol. 644, no. 1, p. 12032, 2015.

- [28] H. Yang, I. MacLaren, L. Jones, G. T. Martinez, M. Simson, M. Huth, H. Ryll, H. Soltau, R. Sagawa, Y. Kondo, C. Ophus, P. Ercius, L. Jin, A. Kovács and P. D. Nellist, "Electron ptychographic phase imaging of light elements in crystalline materials using Wigner distribution deconvolution," *Ultramicroscopy*, vol. 180, pp. 173-179, 2017.
- [29] R. Ishikawa, E. Okunishi, H. Sawada, Y. Kondo, F. Hosokawa and E. Abe, "Direct imaging of hydrogen-atom columns in a crystal by annular bright-field electron microscopy," *Nature Materials*, vol. 10, no. 4, pp. 278-281, 2011.
- [30] J. Song, C. S. Allen, S. Gao, C. Huang, H. Sawada, X. Pan, J. Warner, P. Wang and A. I. Kirkland, "Atomic Resolution Defocused Electron Ptychography at Low Dose with a Fast, Direct Electron Detector," *Scientific Reports*, vol. 9, no. 1, p. 3919, 2019.
- [31] M. Sarikaya, "Evolution of resolution in microscopy," *Ultramicroscopy*, vol. 47, pp. 1-14, 1992.
- [32] A. Suzuki, S. Furutaku, K. Shimomura, K. Yamauchi, Y. Kohmura, T. Ishikawa and Y. Takahashi, "High-resolution multislice x-ray ptychography of extended thick objects.," *Physical Review Letters*, vol. 112, no. 5, p. 53903, 2014.
- [33] M. Humphry, B. J. Kraus, A. C. H. Hurst, A. Maiden and J. Rodenburg, "Ptychographic electron microscopy using high-angle dark-field scattering for sub-nanometre resolution imaging," *Nature Communications*, vol. 3, no. 1, pp. 730-730, 2012.
- [34] P. M. Pelz, W. X. Qiu, R. Bücker, G. Kassier and R. J. D. Miller, "Low-dose cryo electron ptychography via non-convex Bayesian optimization," *Scientific Reports*, vol. 7, no. 1, p. 9883, 2017.
- [35] D. Su and Y. Zhu, "Scanning moiré fringe imaging by scanning transmission electron microscopy," *Ultramicroscopy*, vol. 110, no. 3, pp. 229-233, 2010.
- [36] A. Pofelski, S. Y. Woo, S. Löffler, G. A. Botton, B. H. Le, X. Liu, S. Zhao and Z. Mi, "2D strain mapping using scanning transmission electron microscopy Moiré interferometry and geometrical phase analysis," *Ultramicroscopy*, vol. 187, pp. 1-12, 2018.
- [37] P. Xu, R. F. Loane and J. Silcox, "Energy-filtered convergent-beam electron diffraction in STEM," *Ultramicroscopy*, vol. 38, no. 2, pp. 127-133, 1991.
- [38] L. Reimer, I. Fromm and I. Naundorf, "Electron Spectroscopic Diffraction," *Ultramicroscopy*, vol. 32, no. 1, pp. 80-91, 1990.
- [39] A. Howie, "Inelastic Scattering of Electrons by Crystals I. The Theory of Small-Angle Inelastic Scattering," *Proceedings of the Royal Society of London A: Mathematical, Physical and Engineering Sciences*, vol. 271, no. 1345, pp. 268-287, 1963.

- [40] Z. Wang and J. Cowley, "Simulating high-angle annular dark-field stem images including inelastic thermal diffuse scattering," *Ultramicroscopy*, vol. 31, no. 4, pp. 437-454, 1989.
- [41] A. Maiden, M. Humphry, M. Sarahan, B. Kraus and J. Rodenburg, "An annealing algorithm to correct positioning errors in ptychography.," *Ultramicroscopy*, vol. 120, pp. 64-72, 2012.
- [42] K. Watanabe, T. Yamazaki, I. Hashimoto and M. Shiojiri, "Atomic-resolution annular dark-field STEM image calculations," *Physical Review B*, vol. 64, no. 11, p. 115432, 2001.
- [43] H. Horiuchi, A. J. Schultz, P. C. W. Leung and J. M. Williams, "Time-of-flight neutron diffraction study of a single crystal of yttria-stabilized zirconia, $Zr(Y)O_{1.862}$, at high temperature and in an applied electrical field," *Acta Crystallographica Section B-structural Science*, vol. 40, no. 4, pp. 367-372, 1984.
- [44] Y. S. G. Nashed, D. J. Vine, T. Peterka, J. Deng, R. Ross and C. Jacobsen, "Parallel ptychographic reconstruction," *Optics Express*, vol. 22, no. 26, pp. 32082-32097, 2014.
- [45] T. Latychevskaia, "Iterative phase retrieval in coherent diffractive imaging: practical issues," *Applied Optics*, vol. 57, no. 25, pp. 7187-7197, 2018.
- [46] H. Wang, S. G. Xiao, Q. Xu, T. Zhang and H. Zandbergen, "Fast Preparation of Ultrathin FIB Lamellas for MEMs-Based In Situ TEM Experiments," *Materials Science Forum*, vol. 850, pp. 722-727, 2016.